Forschungszentrum Karlsruhe
in der Helmholtz-Gemeinschaft

Wissenschaftliche Berichte

FZKA 7489

Surface Science Investigations on Spent Nuclear Fuel Model Systems

A. Seibert, S. Stumpf, D. Schild, T. Gouder, D. Bosbach

Institut für Nukleare Entsorgung

Institute for Transuranium Elements
Joint Research Centre, European Commission

Oktober 2009

Forschungszentrum Karlsruhe

in der Helmholtz-Gemeinschaft

Wissenschaftliche Berichte

FZKA 7489

Surface science investigations on spent nuclear fuel model systems

A. Seibert, S. Stumpf, D. Schild, T. Gouder, D. Bosbach

Institut für Nukleare Entsorgung, Forschungszentrum Karlsruhe GmbH

Institute for Transuranium Elements, Joint Research Centre, European Commission

Forschungszentrum Karlsruhe GmbH, Karlsruhe

2009

Für diesen Bericht behalten wir uns alle Rechte vor

Forschungszentrum Karlsruhe GmbH
Postfach 3640, 76021 Karlsruhe

Mitglied der Hermann von Helmholtz-Gemeinschaft
Deutscher Forschungszentren (HGF)

ISSN 0947-8620

urn:nbn:de:0005-074890

Summary

The described research work is motivated by the common interest of SKB (Svensk Kärnbränslehantering AB), INE (Institute for Nuclear Waste Disposal) and ITU (Institute for Transuranium Elements) concerning the mechanistic understanding of the corrosion properties of nuclear waste systems.

The systems investigated are thin films of UO_{2+x} and ThO_2 produced by the sputter deposition technique at ITU and reference materials. Characterisation methods for the films and references are X-ray photoelectron spectroscopy (XPS), X-ray diffraction (XRD) and Atomic Force Microscopy (AFM). Raman microprobe spectroscopy was evaluated as additional examination method for the thin films and surface secondary phases, which can build up during corrosion experiments. The solubility of selected thin film samples was compared to corresponding powder material.

Oberflächenanalytische Untersuchungen an Modellsystemen für abgebrannten Kernbrennstoff

Zusammenfassung

Die beschriebenen Untersuchungen ergaben sich aus einem gemeinsamen Forschungsinteresse von SKB (Svensk Kärnbränslehantering AB), INE (Institut für Nukleare Entsorgung) and ITU (Institut für Transurane) zum mechanistischen Verständnis der Korrosionseigenschaften von abgebranntem Kernbrennstoff.

Die hier untersuchten Systeme sind mittels Sputtertechnik an ITU hergestellte dünne Filme von $UO_{2(+x)}$ und ThO_2 sowie Referenzmaterialien. Diese Systeme wurden mit Röntgen-Photoelektronenspektroskopie (XPS), Röntgendiffraktometrie (XRD) und Rasterkraftmikroskopie (AFM) untersucht. Die Ramanspektroskopie wurde auf ihre Anwendbarkeit als zusätzliche Charakterisierungsmethode für die hergestellten dünnen Filme und Oberflächenpräzipitate untersucht. Einige der hergestellten dünnen Filme sowie herkömmliche Pulverproben wurden auf ihr Löslichkeitsverhalten untersucht.

TABLE OF CONTENTS **PAGE**

1 Introduction 1

2 Experimental 2
2.1 Sample preparation 2
2.1.1 Reference materials 2
2.1.2 Reactive DC sputtering 2
2.1.3 Corrosion experiments 4
2.2 Sample characterisation methods 5
2.2.1 XRD characterisation 5
2.2.2 XPS characterisation 5
2.2.3 AFM characterisation 6
2.2.4 Raman spectroscopic measurements 6
2.2.5 ICP-MS measurements 6
2.2.6 Others 7
2.3 Chemicals 7

3 Results 7
3.1 XRD 7
3.1.1 Thorium dioxide 7
3.1.2 Uranium dioxide 11
3.2 XPS 14
3.2.1 Thorium samples 14
3.2.2 Uranium samples 16
3.3 AFM 19
3.3.1 General considerations 19
3.3.2 Measurements in contact mode 19
3.3.2.1 AFM measurements on ThO_2 thin films 19
3.3.2.2 AFM measurements on UO_2 thin films 21
3.3.3 Measurements in tapping mode 23
3.4 Raman microprobe measurements 25
3.4.1 Testing the depth resolution 26
3.4.2 Reference spectra from bulk powders 28
3.4.2.1 Thorium compounds 28
3.4.2.2 Uranium Compounds 31
3.4.3 Thin film samples 33
3.4.3.1 Uranium dioxide 33
3.4.3.2 Thorium dioxide 36
3.4.4 Surface enhanced Raman spectroscopy (SERS) 39
3.5 Corrosion / solubility experiments with thin film samples 42
3.5.1 Thorium 42
3.5.2 Uranium 47

4 Conclusions 49

5 References 51

Annex A Reference Raman data from literature 56

Annex B Results from solubility experiments 62

LIST OF TABLES

Tab. 1 Synopsis of reference samples. 2
Tab. 2 Synopsis of investigated thin films. 3
Tab. 3 Synopsis of samples and corrosion conditions. 4
Tab. 4 Synopsis of XPS results for ThO_2 films deposited on SiO_2 glass substrates. 16
Tab. 5 Synopsis of AFM results for ThO_2 films deposited on SiO_2 glass substrates. 25
Tab. 6 Raman frequencies for Th compounds from this study. 30
Tab. 7 Raman frequencies for uranium compounds from this study. 31
Tab. 8 Synopsis of the Raman shifts for the ThO_2 thin film samples on SiO_2 glass. 39
Tab. 9 Synopsis of SERS samples and preparation procedure. 41
Tab. 10 Synopsis of AFM results for ThO_2 films deposited on SiO_2 glass substrates before and after the solubility experiments. 46

LIST OF TABLES IN APPENDICES

Tab. 11 Raman shifts from literature for ThO_2 together with our own results. 57
Tab. 12 Raman shifts for uranium compounds from literature and this study. 58
Tab. 13 Blank samples for solubility experiments. 63
Tab. 14 Thorium samples from solubility experiments. 64
Tab. 15 Uranium samples from solubility experiments. 65

LIST OF FIGURES

Fig. 1 Diffractograms of the ThO_2 samples deposited at different deposition rates. 10
Fig. 2 Diffractograms of the UO_2 samples deposited at medium deposition rate at different temperatures. 11
Fig. 3 Diffractograms of UO_2 thin film samples deposited at high deposition rates on two different Au substrates. 12
Fig. 4 Diffractograms of a UO_2 thin film (Au-1) kept under laboratory conditions for 2.4 years. 14
Fig. 5 PE spectra of ThO_2 thin film samples deposited at medium and low deposition rates at RT (30 – 50 °C) and 320 °C on SiO_2 glass substrates (ThO_2-1 to ThO_2-4). 15
Fig. 6 XPS and UPS spectra for UO_2 thin films produced at different temperature: room temperature (RT) and 300 °C. 17
Fig. 7 PE spectra (U-4f and O-1s lines) of a UO_2 thin film sample deposited as stoichiometric UO_2 and after several days under laboratory conditions. 18
Fig. 8 AFM pictures of ThO_2 samples measured in contact mode. 20
Fig. 9 AFM pictures of UO_{2+x} samples on SiO_2 glass substrates measured in contact mode. 21

Fig. 10 AFM pictures of UO_{2+x} samples on Au substrates (SiO_2 piezocrystal electrodes) measured in contact mode or in tapping mode. 22
Fig. 11 AFM image of a UO_{2+x} sample on an Au plate measured in contact mode (Au-2). 22
Fig. 12 AFM images of a ThO_2 thin film surface (ThO_2-2) measured in contact and tapping mode. 23
Fig. 13 AFM images of ThO_2 samples at different deposition temperatures: room temperature, RT (ThO_2-2), 200 °C (ThO_2-6) and 320 °C (ThO_2-4). 24
Fig. 14 Sample arrangement measured for testing the depth resolution. 26
Fig. 15 Raman spectra from different depth in the SiO_2 crystal in the sample arrangement shown in Figure 14. 27
Fig. 16 Depth profiling measurements for the sample arrangement shown in Figure 14 for different lenses and excitation wavelengths. 28
Fig. 17 Raman spectra for the Th compounds. 29
Fig. 18 Raman spectra of meta-schoepite reference samples. 32
Fig. 19 Raman spectra of uranium oxide reference samples: Na- and Ca-Uranate ($Na_2U_2O_7$ * H_2O, CaU_2O_7 * $3H_2O$). 33
Fig. 20 Raman spectrum of a UO_2 thin film on gold substrate. 34
Fig. 21 Example for significant alteration of the thin film samples due to incident laser light. 35
Fig. 22 Raman spectrum of an aged UO_2 thin film on gold substrate. 36
Fig. 23 Raman spectra of ThO_2 thin films on Au. 37
Fig. 24 Raman spectra of ThO_2 thin films on SiO_2 glass. 38
Fig. 25 Raman spectrum of an oxidized UO_2 film without and with silver deposition. 40
Fig. 26 Raman spectra of ThO_2 thin film on SiO_2 glass original and with sputter deposited Au film. 41
Fig. 27 Solubility of ThO_2(cr) samples in different media and leaching times. 44
Fig. 28 AFM images of ThO_2 thin films (deposited at room temperature and 200 °C) before and after a solubility experiment over 25 days in carbonate buffer. 45
Fig. 29 Solubility of $UO_{2(+x)}$ thin film samples in different media and on different substrates. 47
Fig. 30 Raman spectra of a $UO_{2(+x)}$ thin film on gold substrate (Au-3) before (A) and after (B) the solubility experiment in the phosphate electrolyte, pH 7.6. 48
Fig. 31 Raman spectra from precipitate and reference spectra of hematite. 49

1 Introduction

For a reliable assessment of the long-term storage behaviour of spent nuclear fuel a mechanistic understanding of the interactions of the waste forms with the surrounding environment is indispensable. A potential failure of the technical barriers can result in contact of the fuel matrix with groundwater. The formation of higher actinide oxides from the dioxide fuels or waste forms (UO_2 and PuO_2 or mixed oxides) directly influences the dissolution behaviour of the spent fuel and is therefore of special interest in the context of nuclear waste disposal [Bru06]. As the actinide dioxides AnO_2 show a very low solubility under reducing conditions expected for the potential deep geological repositories they may be considered as an efficient barrier. Anyhow, under possibly oxidizing conditions and considering the radiolysis of the contacting groundwater due to the inherent radioactivity of the spent nuclear fuel the fuel matrix will undergo an oxidation from the tetravalent state An(IV) to the significantly more soluble An(V / VI). This corrosion process will lead to dissolution of the fuel and therewith the release of radionuclides from the matrix to the environment. The dissolution of UO_2 and UO_2 based spent fuel have been extensively studied over the last years and led to some agreement on the elementary reactions involved in the overall process [Spa00, Spa04]. But the spent fuel system is very complex and it is difficult to draw conclusions on the mechanisms from experiments with this complex systems. Therefore laboratory experiments using simple model systems for single effect studies were adopted to elucidate the underlying mechanistic processes of the overall dissolution process. With this approach several key reactions within a failed container in contact with groundwater were identified and are widely agreed on, but a complete understanding necessary for long term predictions is not achieved yet [Spa04]. Contrary to the vast data on various aspects of UO_2 and UO_2 spent fuel corrosion the current data concerning the behaviour of MOX fuel under conditions expected in case of the failure of the technical barriers [Sho00, Sho07, Ser98, Gla00, Jeg04, Joh05] is inadequate for reliable performance assessment. These actual or advanced nuclear fuels are made of solid solution UO_2-PuO_2, ThO_2-UO_2 and ThO_2-PuO_2 [Hub08a]. The interest in thorium-based fuel for Generation IV nuclear energy systems was renewed in the past few years. But as well in this case the investigations on their behaviour in aqueous solution is very limited [Ser98, Fou00, Hei03, Hei04, Dem04, Smi04, All05, Hub08a, Hub08b].

This exploratory investigation is a first step to the investigations planned in the frame of a 3-years project between INE, SKB and ITU. It is focused on the evaluation of surface analytical techniques available at INE and ITU for the characterisation of the thin film fuel model systems. Here especially Photoelectron spectroscopy with X-ray excitation (XPS), Atomic Force Microscopy and Raman spectroscopy are in the focus. As additional technique, X-ray diffraction (XRD) is used for the thin film characterisation. For this preliminary investigation we confine ourselves on samples with low complexity that can be used in the future as reference base for the mixed oxide systems.

2 Experimental

2.1 Sample preparation

2.1.1 Reference materials

Some well characterised uranium oxides and thorium oxides (powder samples) are used as reference materials for comparison reason. The materials are summarised in Table 1. Also all thin film substrates used in the sample production are investigated as blank tests (SiO_2(cr), SiO_2 glass, Au deposit on SiO_2(cr) (microbalance crystal), Au foil, Au plates).

Table 1: Synopsis of reference samples.

Sample	**Characterisation**
ThO_2 (cr)	cert. material 99.99 % (Alfa Aesar), XRD
$Th(OH)_4$	precipitate from alkaline Th^{4+} solution, XRD
$Th(OH)_4$ calcined	Calcined product at 1100°C
UO_2	Thin film, XPS
U_3O_8 (10% UO_2)	XRD
Metaschoepite	XRD
Na-Uranate	XRD
Ca-Uranate	XRD

2.1.2 Reactive DC sputtering

The ThO_2 and UO_2 films are prepared by direct-current sputter deposition from the according metal targets (U_{nat} disk, resp. Th-232 disk) with an Ar/O_2 mixture as sputter gas, respectively reaction gas. The plasma in the diode source is maintained by injection of electrons of 50 – 100 eV energy. This allows a low sputter gas pressure of ~ 1 - 2 Pa. The background pressure in the preparation chamber varied over the time, but never exceeded $2.7 \cdot 10^{-6}$ Pa. The metal target is held at - 800 V. No sample bias is applied. Different substrates are used: quartz glass plates, gold (foil or plate) and quartz crystals with a Au/Ti(Cr) deposit which are usually used in the electrochemical quartz microbalance system (ECQM). All samples with their production parameters are summarised in Table 2.

Table 2: Synopsis of investigated thin films.

		Deposition conditions					
sample name	expected film com-position	substrate	T, °C	target current, mA	O_2 pressu-re, Pa	Ar pressu-re, Pa	Mass, μg *(values) are measured, others are estimates
Thorium							
ThO_2-1	ThO_2	SiO_2	RT	1.1	0.013	1.640	150
ThO_2-2	ThO_2	SiO_2	RT	3.5	0.013	1.681	350 (320)*
ThO_2-3	ThO_2	SiO_2	320	1.2	0.013	1.968	150
ThO_2-4	ThO_2	SiO_2	320	3.4	0.013	1.517	350
Cr20	ThO_2	ECQM	50	3.8	0.007	4.000	300
Cr23	ThO_2	ECQM	50	3.8	0.007	4.500	300
ThO_2-5	ThO_2	SiO_2	200	1.1	0.013	1.681	100 (91)*
ThO_2-6	ThO_2	SiO_2	200	3.5	0.013	1.558	250 (250)*
ThO_2-7	ThO_2	SiO_2	RT	1.2	0.013	1.968	100
ThO_2-8	ThO_2	SiO_2	RT	3.4	0.013	1.517	250
Uranium							
SiO_2-1	UO_{2+x}	SiO_2	50	2.4	0.004	3.800	150
SiO_2-2	UO_{2+x}	SiO_2	260	2.4	0.004	3.450	(152)*
SiO_2-3	UO_{2+x}	SiO_2	260	2.4	0.004	3.650	(127)*
Crold1	UO_{2+x}	ECQM	55	3.8	0.011	4.550	(120)*
Cr50	UO_{2+x}	ECQM Au/SiO_2	55	~ 4	0.007	4.200	900
Au-1	UO_{2+x} (U_{met})	Au plate	55	3.9	0.005	3.200	900
Au-2	UO_{2+x}	Au plate	55	3.9	0.005	6.000	900
Au-3	UO_{2+x}	Au foil	50 250 550	2.3	0.004	3.250	(170)*
UO_2-1	UO_2	Au foil	200	Not comparable			n.d.

2.1.3 Corrosion experiments

Some of the above listed samples are selected for corrosion experiments. Sample names and corresponding corrosion conditions are summarised in Table 3. Results from ICP-MS measurements are given in the annex together with results from blank samples.

Table 3: Synopsis of samples and corrosion conditions. g: glass vial, PE: PE vial.

Corrosion conditions								
sample name	expected film composition	substrate	vial	solution	atmosphere	volume, ml	mass, µg *(values) are measured, others are estimates	pH
Thorium								
A	ThO_2 (cr)	-	g	NaCl	Ar	15	$(2.2 \cdot 10^4)$*	6
B	ThO_2 (cr)	-	g	phos	Ar	15	$(1.4 \cdot 10^4)$*	7.6
C	ThO_2 (cr)	-	g	carb	air	15	$(3.6 \cdot 10^4)$*	9.3
D	ThO_2 (cr)	-	PE	NaCl	Ar	15	$(1.3 \cdot 10^4)$*	6
E	ThO_2 (cr)	-	PE	phos	Ar	15	$(1.6 \cdot 10^4)$*	7.6
F	ThO_2 (cr)	-	PE	carb	air	15	$(1.6 \cdot 10^4)$*	9.3
Cr23	ThO_2	ECQM	PE	NaCl	Ar	5	300	6
ThO_2-5	ThO_2	SiO_2	PE	phos	Ar	5	(91)*	7.6
ThO_2-6	ThO_2	SiO_2	PE	carb	air	5	(250)*	9.3
ThO_2-7	ThO_2	SiO_2	PE	phos	Ar	5	100	7.6
ThO_2-8	ThO_2	SiO_2	PE	carb	air	5	250	9.3
Uranium								
SiO_2-2	UO_{2+x}	SiO_2	PE	NaCl	air	5	(152)*	6
SiO_2-3	UO_{2+x}	SiO_2	PE	NaCl	air	5	(127)*	6
Crold1	UO_{2+x}	ECQM	PE	phos	Ar	5	(120)*	7.6
Cr50	UO_{2+x}	ECQM	PE	carb	air	15	900	9.3
Au-2	UO_{2+x}	Au plate	PE	carb	air	5	900	9.3
Au-3	UO_{2+x}	Au foil	PE	phos	Ar	15	(170)*	7.6
Blanks								
Glass 1	-	SiO_2	PE	carb	air	5		9.3
Glass 2	-	SiO_2	PE	phos	Ar	5		7.6
Glass 3	-	-	g	phos	Ar	5		7.6
Glass 4	-	-	g	carb	air	5		9.3
Glass 5	-	-	g	NaCl	air	5		6

The corresponding aqueous solutions are as follows:

NaCl: 0.01 M NaCl, pH_{meas} = 6.0

phos: $3.3 \cdot 10^{-4}$ M total phosphate concentration with $[H_2PO_4^-] = 6.7 \cdot 10^{-5}$ M, $[HPO_4^{2-}] = 2.7 \cdot 10^{-4}$ M, pH_{meas} = 7.6, I = 0.01 M (NaCl)

carb: $9.5 \cdot 10^{-3}$ M total carbonate concentration with $[CO_3^{2-}] = 9 \cdot 10^{-4}$ M, $[HCO_3^-] = 8.6 \cdot 10^{-3}$ M, pH_{meas} = 9.3, I ~ 0.01 M ($NaHCO_3/Na_2CO_3$)

Samples are left for 18.5 d (and/or 25d) under two different atmospheric conditions: air means laboratory atmosphere. The used $NaHCO_3/Na_2CO_3$ buffer is near the carbonate equilibrium condition for air, whereas the NaCl electrolyte is thought to be stable against massive carbonate intrusion as it is handled in closed vessels. Ar means the experiments are conducted in an Ar glove box with nominal O_2 content below 1 ppm and a CO_2 content < 0.1 ppm.

Different vials (glass and PE) are used in the reference experiments with ThO_2 (cr) to check for an influence of silicate on the reactions as the substrates used for the thin films are SiO_2 glass or quartz.

Ultracentrifugation (1h, 90000 rpm, resp. $5 \cdot 10^5$ g) was used as phase separation method only for few samples.

2.2 Sample characterisation methods

2.2.1 XRD characterisation

XRD experiments are performed on a diffractometer equipped with θ / 2θ -goniometer, a Philips PW3830 High Voltage Generator and a Philips PW2213/20 XRD Glass X-Ray tube (Cu K_α, 8048.0 eV). The detector is a scintillation counter SZ20/SE from Seifert, Ahrensburg. A home made control program manages the goniometer controlling and the data acquisition. Additionally a Bruker D8 diffractometer with rotating sample holder equipped with a Bruker Si(Li) solid state detector is used for some samples. All experiments are performed in the Bragg-Brentano mode.

2.2.2 XPS characterisation

XPS spectra are recorded using a Leyboldt LHS-10 hemispherical analyzer or a multichannel hemispherical analyzer EAC2000-125 from Omicron. Mg K_α (1253.6 eV), Al K_α (1486.6 eV) excitation radiation or UV radiation (He II radiation with 40.8 eV) is used. The background pressure in the analysis chamber normally is around $5 \cdot 10^{-8}$ Pa. Calibration is done regularly using the Au-4f levels of a sputter cleaned Au plate with a binding energy of 84.0 eV ($4f_{7/2}$) and the Fermi edge detected in the UV photoelectron spectrum.

2.2.3 AFM characterisation

Samples are measured using the commercial AFM instruments Explorer (Topometrix) or Dimension 3000 (Digital Instruments). DNP Tips, Veeco NanoProbe, are used (Si nitride) with a nominal tip radius, R, of 20 nm (R_{max} = 40 nm). The 200 μm cantilever with wide arms is used (nominal spring constant: 0.12 $N \cdot m^{-1}$) for contact mode measurements. In Tapping mode RTESP tips with a cantilever made from phosphorus doped Si (Veeco NanoProbe) are used. They have a nominal tip radius R = 8 nm (R_{max} = 10 nm) and a nominal resonance frequency f_0 = 300 kHz. The microscopic pictures were evaluated and quantified using WSxM 4.0 Develop 9.3 software (Nanotec Electronica S.L.)[Hor07].

In contact mode AFM, the tip is in perpetual contact with the sample surface and is gently traced across it (X-Y-direction). The contact force causes the cantilever to bend and a Z-feedback electronic loop works to maintain a constant cantilever deflection. Tapping mode works by lightly tapping the sample surface with an oscillating probe tip. The cantilever is oscillating with a certain frequency in this case and the amplitude (typically above 20 nm without surface contact) of this oscillation is reduced in contact with the sample surface. This change in the amplitude is used to measure the surface features, giving an image of the surface topography. This eliminates much of the lateral forces induced onto the sample surface compared to the contact mode. As well the direct contact with the sample surface is reduced.

2.2.4 Raman spectroscopic measurements

Measurements are performed on a SENTERRA Raman microscope system, developed by Bruker Optics, equipped with an Olympus B51 microscope (10x, 20x and 50x objectives). Raman active vibrations are excited by a laser diode with 785 nm or a frequency doubled Nd-YAG laser with 532 nm. The acquired spectra are in the range between 80 and 4000 cm^{-1} with a spectral resolution ~ 3 cm^{-1}. The wavenumber accuracy (long term stability) is better than 0.1 cm^{-1} due to the Sure-Cal routine used in the instrument. The provided software package OPUS is used operating the instrument, acquiring spectra and for data display and analysis. From each sample two or more spectra are recorded at different locations with a local resolution of about 1 μm (value from specification). The depth resolution with the 50x objective was tested with a SiO_2/polyacrylate system and is not better than 140 μm for the 785 nm excitation wavelength with the used slit system (see below).

The spectra are preferentially measured with 785 nm excitation, because excitation with the 532 nm laser showed in many cases a huge fluorescence even at low wavenumbers superimposing the Raman scattering signal. Also sample degradation (especially for the uranium oxides) is observed at high laser powers for both excitation wavelength.

2.2.5 ICP-MS measurements

ICP-MS is used to determine the thorium, respectively uranium, concentration in solution. As well the Si concentration is determined. Measurements are performed with an ELAN 6100, Perkin Elmer. Sample aliquots are diluted by a factor of ten into 2% HNO_3. Only single diluted samples are measured.

2.2.6 Others

pH_c values are determined with combination pH electrodes (ROSS-type, Orion Co.) calibrated with buffer solutions of pH 4, pH 7 and pH 9 at 22 °C.

2.3 Chemicals

All chemicals used are from Merck, Darmstadt. NaCl, $NaHCO_3$ and Na_2CO_3 are p.a. grade. HNO_3, NaH_2PO_4 and Na_2HPO_4 (both water free) are Suprapur materials. All solutions are prepared with ultrapure water from a water purification apparatus (Milli-Q, Millipore).

ThO_2 was obtained from Alfa Aesar with 99.99 % purity, $Th(NO_3)_4 \cdot 6H_2O$ p.a. was used (possible impurities: chloride, sulphate, Fe, Ti , Pb, rare earths) for the preparation of $Th(OH)_4$.

A suspension of gold colloids (mean diameter 20.8 nm) in H_2O purchased from BBInternational was tested for SERS measurements as well as Au and Ag coatings deposited from the corresponding metal foils.

3 Results

3.1 XRD

For all thin film samples diffractograms with distinct peaks are obtained after production, showing that they are crystalline. A cubic pattern is determined for the fresh samples with nominally UO_2, UO_{2+x} and ThO_2 composition. Anyhow the usual intensity ratios obtained from powder samples are not reproduced. Depending on the deposition conditions a preferential orientation is obtained.

3.1.1 Thorium dioxide

The diffractograms for the ThO_2 samples on SiO_2 glass substrates are shown in Figure 1. For room temperature (RT) condition the (200) diffraction peak is preferred, as well (311) is significant. It is not clear why this is the case. For UO_2 depositions (with comparable deposition rates, and substrates, SiO_2 and Au) a distinct pronounciation of the (111) diffraction peak is found, which increases by increasing the deposition rate or temperature [Sei07]. This preferred orientation is explained by the fact, that higher deposition rates (many atoms impinging on a surface area: shorter ways) and higher temperatures (surface adatoms are more mobile) increase the probability of atoms to hit together during a given time, therewith allowing them to reach a more favourable energetic state faster. In case of UO_2 the (111) surface with the lowest surface energy of all the crystal planes ((111) < (110) < (100)) is expected to build up preferentially then. According to the isostructural crystal lattice of ThO_2 one would expect the same behaviour for the two oxides, which is not evident in those first deposition tests: With increasing temperature (320 °C) (111) and (220) diffraction peaks become more pronounced and (200) is significantly suppressed. The (311) diffraction peak is still significant for the increased temperature. All other diffraction peaks are less pronounced (therefore the plotted 2θ region in Figure 1 is confined to values below 70 °). Some significant differences

between medium and low deposition rates are observed. At RT the (111) and (220) diffraction peaks are less pronounced for the higher deposition rates, whereas it seems that the (200) and (311) diffraction peaks increase more than the others for the higher deposition rate (quite different than in the UO_2 case). For the samples heated to 320 °C a similar effect between (111) / (220) and (200) / (311) is observed, with now (111) / (220) increasing more in intensity with increasing deposition rate than the other two diffraction peaks. Additionally, for the low deposition rate sample an asymmetric shape of the peaks is observed, with a shoulder at low 2θ values and a maximum at higher 2θ values as that observed for the more symmetric diffraction peaks of the sample with high deposition rate. The 200 °C samples seem to be somewhere in between the two extreme cases: the (200) diffraction peak is strongly decreased compared to the RT samples. On the other hand, this peak together with the (311) peak, increases more than proportional for the high deposition rate samples as seen for the RT samples. The strong increase in intensity, seen for the (111) and (220) diffraction peaks at 320 °C substrate temperature, is not observed for the 200 °C sample.

Similar diffractograms, with significant pronounciation of the (200) diffraction peak, are observed for depositions at RT on the gold layer of the electrochemical quartz crystal microbalance (ECQM) substrates (not shown here). This again is in accordance with the behaviour observed for UO_2 deposits, that the substrate does not play an important role as structure template under these deposition conditions. Probably the surface roughness influences this behaviour (see 3.1.2). An explanation for the different behaviour of the two oxides (Th and U) is not completely clear up to now. The melting temperatures, T_m, (3220 °C for ThO_2 and 2847 °C for UO_2) that play a role in the structural zone models (originally developed to describe the sputtering process of metals [Tho74, Tho77]) are not extremely different. In this model usually the ratio of substrate temperature normalised to the melting point of the sputtered film material is used to describe the development of grain morphology with temperature and other deposition parameters, giving a consistent picture for different materials. Anyway, this normalisation only leads to a slight difference for T/T_m, 0.16 (ThO_2) compared to 0.18 (UO_2). Indeed, the more important factor for a preferential orientation should be the balance between surface energy and bulk free energy differences between the grains with different orientation. Surface energy is the excess energy per unit area as compared to the bulk structure. Surface energy trends, calculated consistently in [Sko08] for both oxides show that for UO_2 and ThO_2, as expected for isostructural oxides, the (111) surfaces have the lowest surface energy compared to (110) and (100). Therewith the (111) surface is considered the most stable surface termination under vacuum conditions for both oxides [Sko08, Abr01]. Absolute values for the surface energies for all three planes are slightly higher for ThO_2 than for UO_2. Comparing different slab thicknesses for the calculations in [Sko08] it is seen that with increasing slab thickness (going towards bulk) the surface energy levels off (or is even increasing) for ThO_2 whereas for UO_2 it tends to decrease. This is attributed to the semiconducting property of UO_2 that lessens the effect of dangling bonds at the surface by a redistribution of the electron density (lowering the surface energy). ThO_2 due to its different electronic structure (no 5f electrons in the valence band compared to two unpaired 5f electrons in the valence band for UO_2) is an insulator with a band gap of ~6 eV which does not allow such electron redistribution. A stabilisation of the other surfaces may be possible by hydroxylation (as found for UO_2 and PuO_2 [Abr01]) or other effects. Total density of states (DOS) calculations for the bulk systems and the (111) surfaces in [Sko08] show distinct differences between ThO_2 and UO_2. For the ThO_2 the band gap for surface and bulk system is

nearly identical as well as the occupation of the bonding orbitals below the Fermi energy. For UO_2 the energy gap between the occupied 5f states and the unoccupied levels in the conduction band increases in the calculation. Also a shift to higher binding energy for the O-2p and U-(6d7s) orbitals is observed. Anyhow the overall similarity between (111) surface DOS and bulk DOS for both oxides should count for the bulk like behaviour of the (111) surface. The bulk free energies of formation, $\Delta_f G_m^0$ [Gre92, Ran08], are different for UO_2(cr) and ThO_2(cr), -1031.8 kJ·mol^{-1}, resp. -1169.0 kJ·mol^{-1}. But as well the particle (or crystallite) size (via the surface area per mole of solid) should influence the Gibbs energy.

The relative high FWHM (full width at half maximum) of the peaks indicates that the crystallites are small. The calculated lattice parameter varies between 5.628 Å and 5.649 Å comparing to 5.600 Å calculated for a ThO_2 sample from literature [Lei74].

Thin films of ThO_2 produced by a completely different technique (spray pyrolysis of Th-nitrate solutions [Mah02]) show under special production conditions (T_s ~ 350 °C, > 0.2 M Th solution, > 100 nm film thickness) as well a crystallised ThO_2 film with the expected cubic pattern and a preferential orientation along the (111) direction.

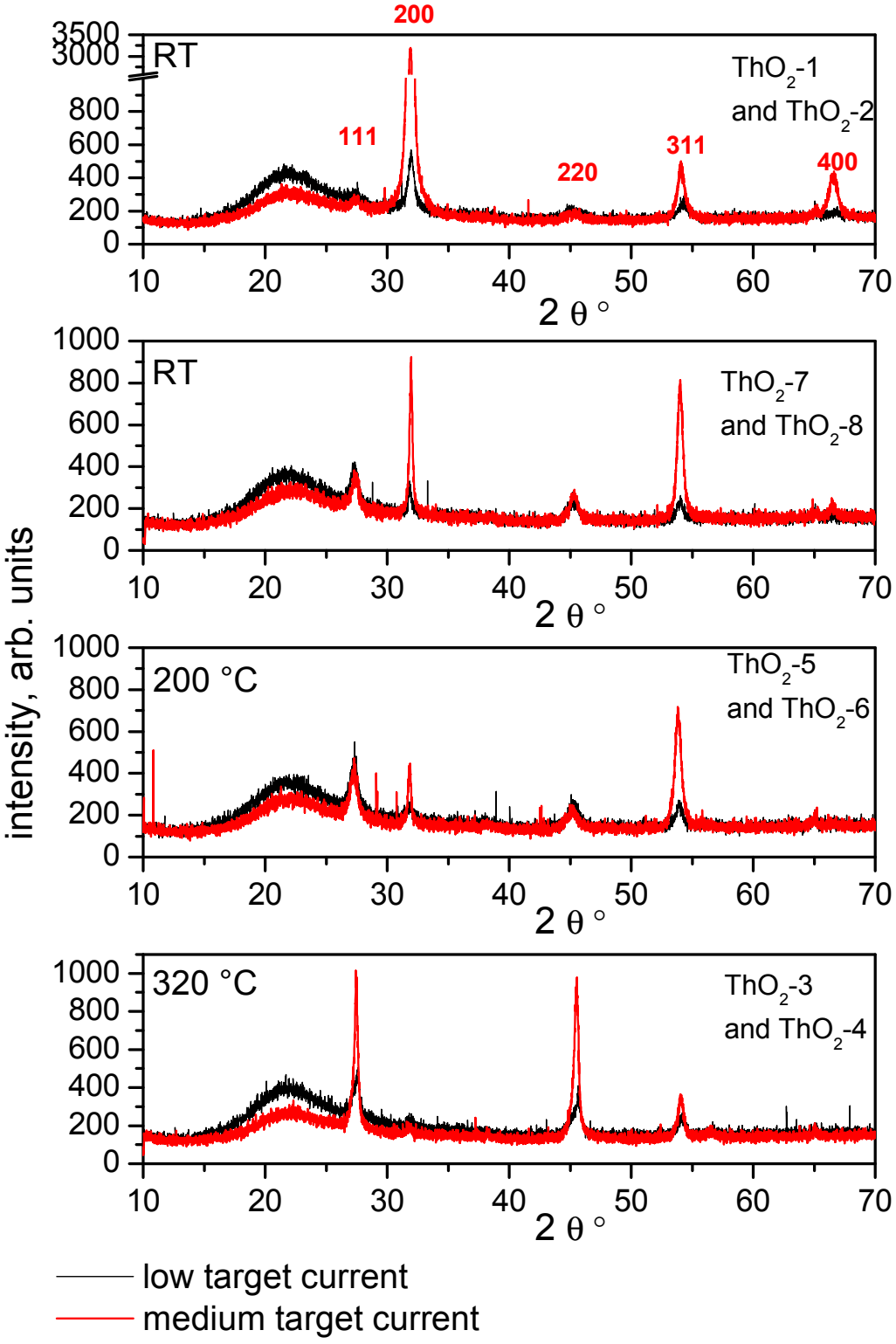

Figure 1: Diffractograms of the ThO_2 samples deposited at different deposition rates (black curves: ~50 $ng \cdot s^{-1} \cdot cm^{-2}$, red curves: ~160 $ng \cdot s^{-1} \cdot cm^{-2}$).

3.1.2 Uranium dioxide

Figure 2 shows the diffractograms for UO_2 thin films on SiO_2 or Au substrates for medium deposition rates (~ 210 $ng \cdot s^{-1} \cdot cm^{-2}$) and different deposition temperatures.

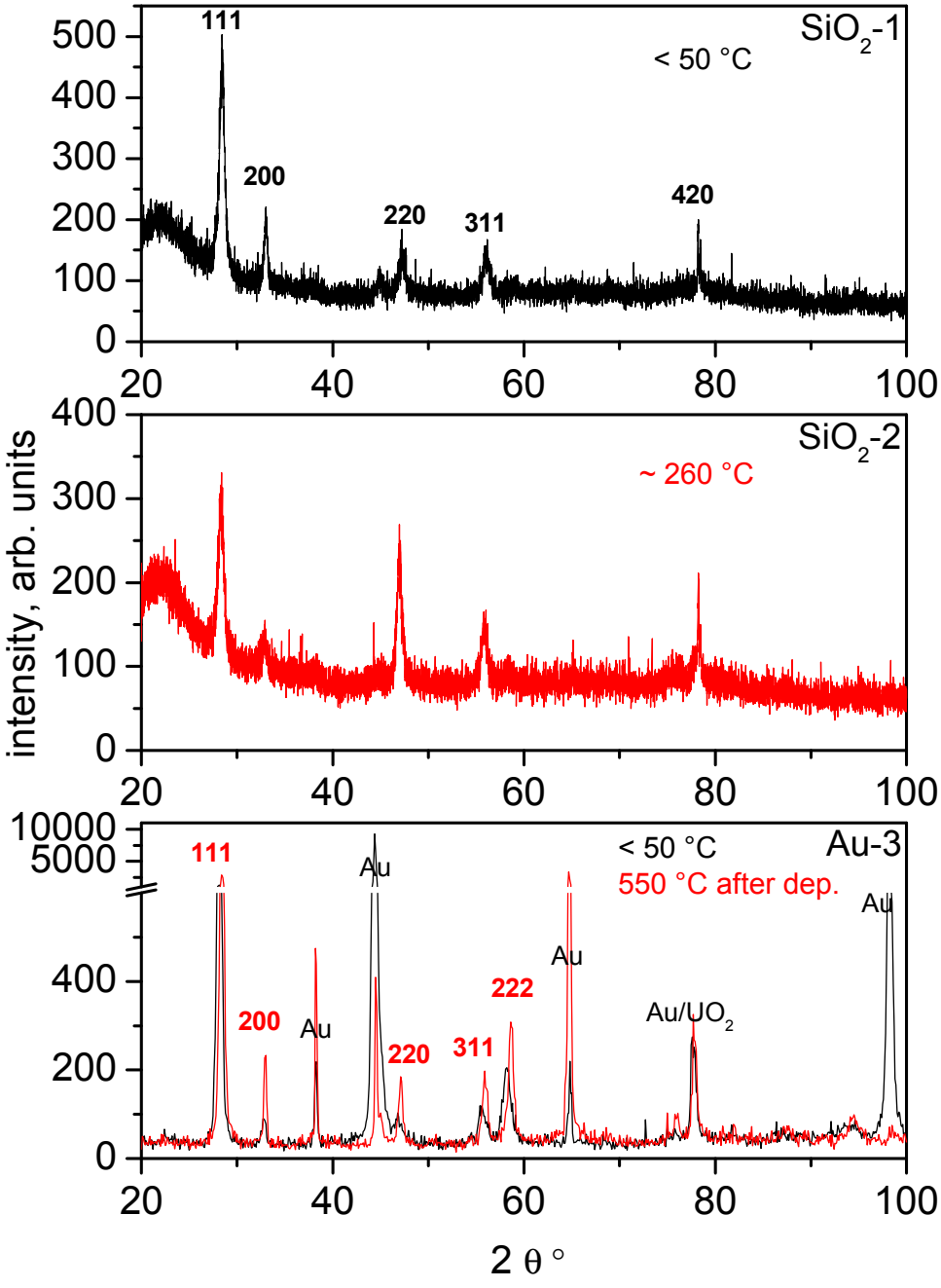

Figure 2: Diffractograms of the UO_2 samples deposited at medium deposition rate at different temperatures (black curves: 30 – 50 °C, red curves: > 250 °C or heated to 550 °C).

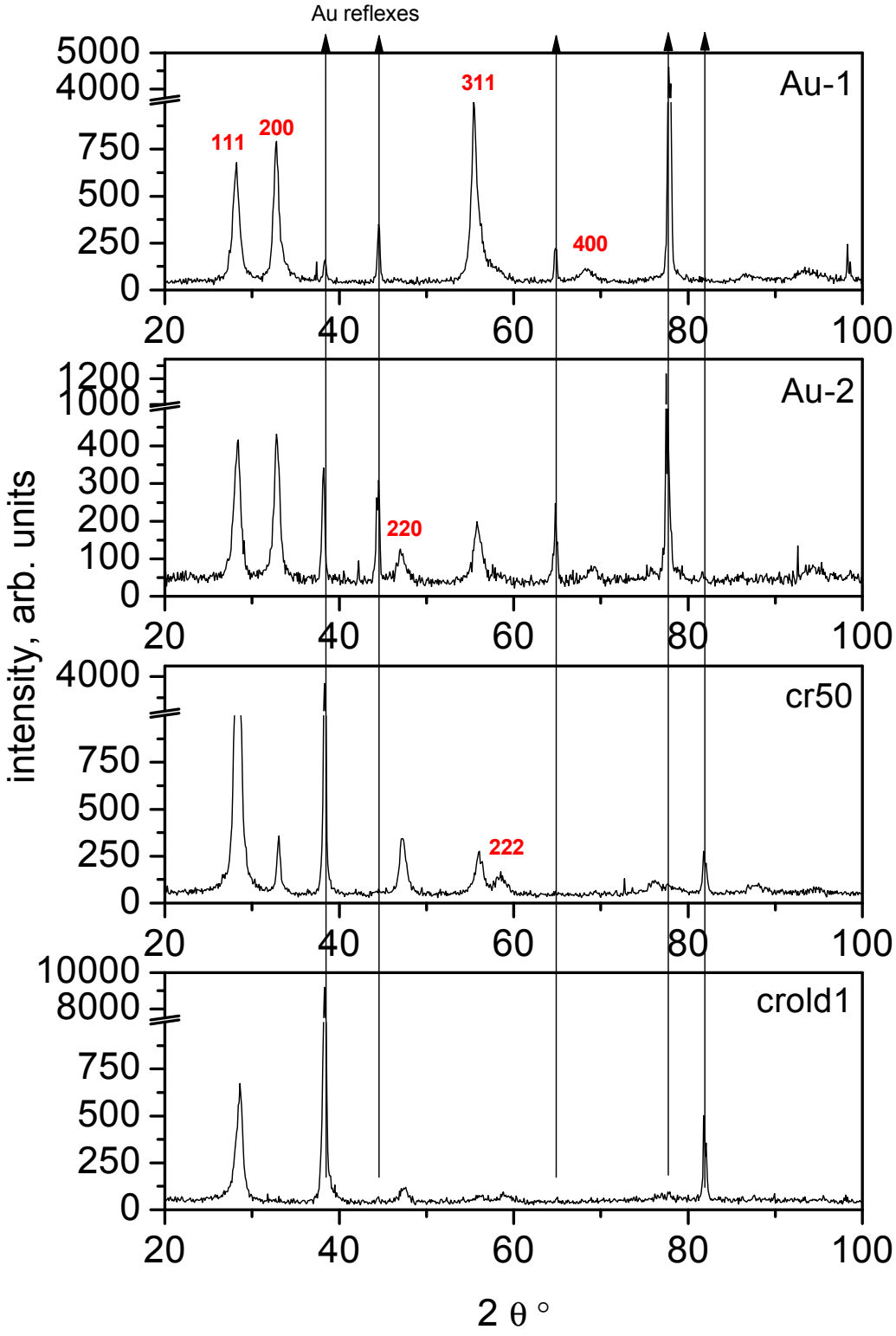

Figure 3: Diffractograms of UO_2 thin film samples deposited at high deposition rates ~ 300 ng·s^{-1}·cm^{-2} at RT (30 – 50 °C) on two different Au substrates (Au-1, Au-2: gold plates; cr50, crold1: Au electrode on ECQM crystal).

The significant different count rates for the intensity values between the samples on SiO_2 and Au are an effect of different film thicknesses. The two samples deposited at RT (Figure 2, black curves) show a comparable intensity distribution with the highest intensity for the (111) diffraction peak, all others are much less pronounced. This was as well observed in an earlier study [Sei07]. For the sample deposited at 260 °C, beside the (111) diffraction peak the (220) peak shows significant intensity, which is not expected from [Sei07].

The heating experiment after the deposition at RT with the film on the gold substrate shows that for the UO_2 film the differences are minor concerning the crystallite orientation in the film. But the diffraction peaks are slightly shifted to higher 2θ values. This corresponds to a smaller lattice parameter and therewith probably a more oxidised bulk sample. The gold diffraction peaks are not shifted in their position due to the heating process, but the intensity ratios for the different diffraction peaks are strongly different before and after the heating step. This may be an effect of relaxation of the oriented structure of the gold foil (introduced by the welding process during the production of the foil) by the heating. Anyhow, after the heating process the (220) diffraction peak shows the highest intensity. This is different to the peak intensity distribution in Au powder samples.

The UO_2 thin film samples on the gold electrodes of the ECQM crystals (cr50, crold1) show indeed a similar behaviour as seen before. With medium and high deposition rates the (111) diffraction peak is strongly preferred (compare Figure 2, black spectra and Figure 3, bottom spectra) independent if the substrate is an amorphous SiO_2 glass, an Au foil or an Au thin film electrode (from PVD technique). An exception from this behaviour is seen in the samples deposited on the gold plates at low temperature, but at high deposition rate (Figure 3, upper spectra: Au-1, Au-2) this preferential orientation is not observed. This may be due to the different surface morphology of the plates. Whereas the SiO_2 glass (thickness 0.15 mm), the deposited Au electrode on the microbalance crystals (0.2 mm) and even the Au foil (0.025 mm) surfaces are very smooth, the polished Au plate (~ 0.2 mm) surfaces still show a strong structuring (cratered and rugged) which may lead to a different growth mechanism or at least different kinetics as observed for the very smooth substrates. Different thermalisation of the deposited atoms on the substrates due to their different thicknesses and / or materials may also play a role.

The alteration of a stoichiometric UO_2 film in air over a period of 882 d was followed with XRD. Figure 4 shows the sample Au-1 measured after production, after 50 d and after 882 d in ambient laboratory atmosphere. After production XPS showed a U-4f level characteristic for stoichiometric UO_2. Also the calculated O/U ratio of 1.95 is in accordance with stoichiometric UO_2. The diffraction pattern at that time is according as well to the cubic pattern of UO_2. The calculated lattice parameter was (5.4859 ± 0.0189) Å compared to (5.4666 ± 0.0026) Å for a reference and a value of 5.4682 Å taken from literature [Coo82]. Only a very slight difference between the diffractograms for the different storage times is seen. Still the diffraction peaks for the cubic UO_2 system are observed but with different intensity than in the beginning, but this is as well true for the diffraction peaks of the underlying gold substrate and therewith not necessarily considered as a significant change but probably due to a different measurement geometry. The same is true for the shift of the diffraction peaks: A shift to higher values of 2θ is observed, but for the UO_2 and Au diffraction peaks (to slightly different extent). Increasing the hyperstoichiometry of UO_2 would lead to such a shift but, due to

the similarly shifted Au peaks, the significance is not necessarily given here. An additional diffraction peak appears 47.5 ° that can be identified as the 220 diffraction peak of UO_2, which was not significant in the first measurements set-up (probably due to the used static sample holder). Although a higher oxidised surface was detected by Raman spectroscopy (see below).

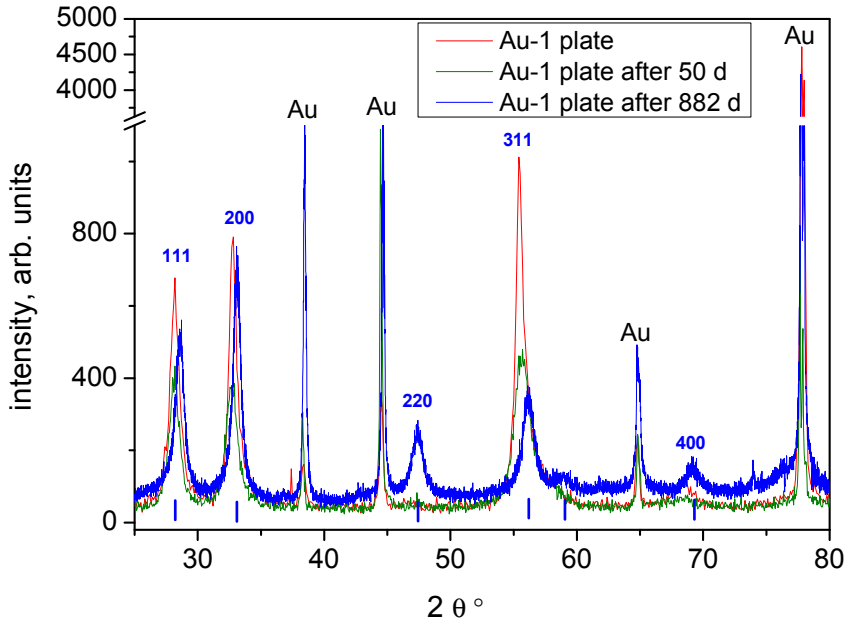

Figure 4: Diffractograms of a UO_2 thin film (Au-1) kept under laboratory conditions for 2.4 y.

3.2 XPS

The samples are measured direct after their production by XPS to determine an initial composition AnO_x. This procedure to calculate the composition (or the O/An ratio, x) leads to values with a relative high uncertainty (± 15 %). The atomic sensitivity factors (ASF) used for this purpose are determined from reference materials ($UO_{2.0}$) or estimated from this by correcting with the photoionisation cross sections as described in [Gou02]. ASF used are 0.66 for O-1s from [Wag81], 12.64 for Th-4f and 13.11 for U-4f, resp. 14.45 depending on the measuring system (mainly the different x-ray excitation sources).

3.2.1 Thorium samples

In Figure 5 the Th-4f and O-1s lines for the samples ThO_2-1 to ThO_2-4 (on SiO_2 glass substrates) are plotted together. These samples cover the complete range of different production parameters target current and temperature. It can be seen that the differences in the Th-4f and O-1s lines are only subtle. In the XPS spectra for room temperature and 320 °C samples a slight difference in the peak width of the Th-4f and O-1s lines is observed: the room temperature samples show Th-4f and O-1s lines with an increased peak width indicating a lower

crystallinity. The samples deposited at the same substrate temperature but with different target currents are similar in shape. Slight shifts in BE (~ 0.4 eV) for the samples with different target currents (corresponding to different deposition rates) may be due to different charging effects as the samples have different film thickness. The overall sample charging of ~ 6 – 7 eV is not corrected for in the plots. O/Th ratios are calculated with the estimated sensitivity factors and vary between 1.97 and 2.22 with no significant dependence on one of the variables. This becomes clear from Table 4 which summarises the XPS results for the thorium samples. For UO_2 it was found that the O/U ratio depended on the deposition temperature [Sei07]. Here the variation of the O/Th ratio does neither depend on the production temperature nor on the target current.

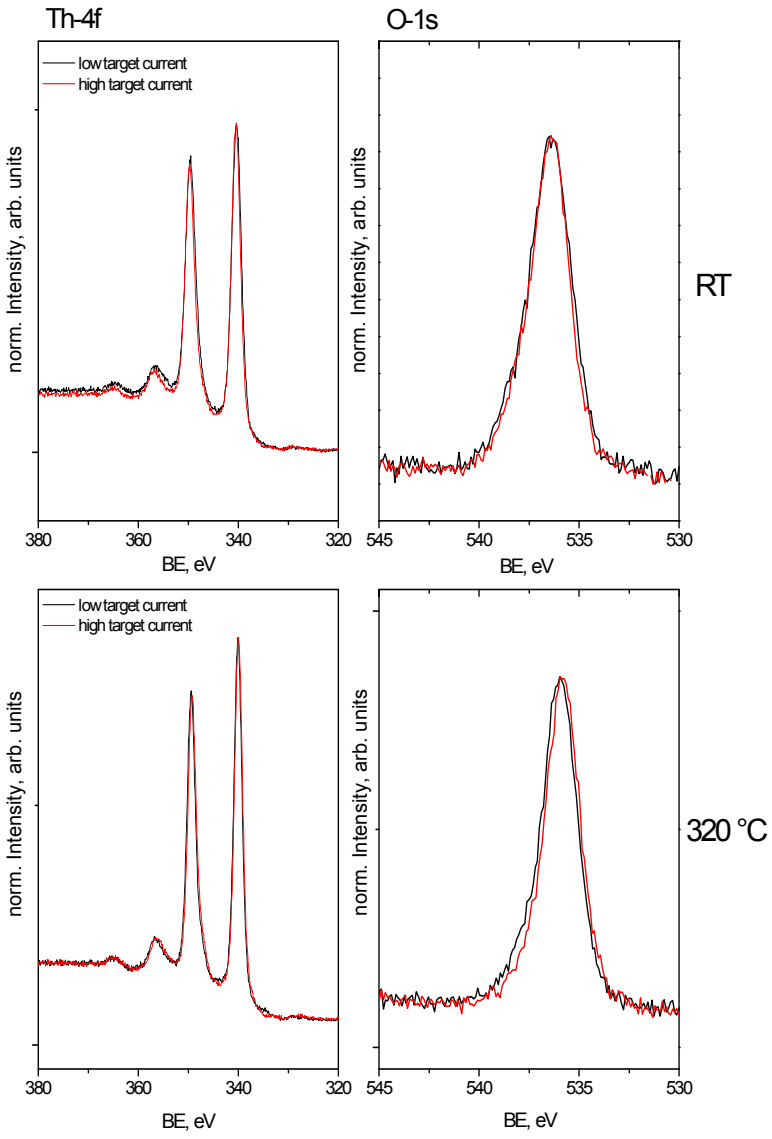

Figure 5: PE spectra of ThO_2 thin film samples deposited at medium and low deposition rates at RT (30 – 50 °C) and 320 °C on SiO_2 glass substrates (ThO_2-1 to ThO_2-4). Excitation source is AlK_α with 1486.6 eV. No charge referencing is applied.

The different target currents, as stated above, correspond to slow and medium deposition rates and (as the deposition times were chosen the same for all depositions) therewith different film thickness. The film thickness was indeed not supposed to have an influence on the composition as usually constant conditions are observed throughout the depositions (gas pressure, currents, voltages).The sputter gas and oxygen pressures were chosen very similar for all depositions and therewith do not belong to the varied parameters.

Table 4: Synopsis of XPS results for ThO_2 films deposited on SiO_2 glass substrates. Marked values* are corresponding to measured deposited mass, other values are estimated from these.

	Deposition conditions				
Sample name	pressure ratio Ar/O_2	T, °C	estimated deposition rate $ng \cdot s^{-1} \cdot cm^{-2}$	estimated film thickness, nm	O/Th
ThO_2-1	126	RT	80	100	1.97
ThO_2-2	129	RT	178*	216*	2.07
ThO_2-3	151	320	80	100	2.07
ThO_2-4	117	320	190	240	2.09
ThO_2-5	129	200	51*	62*	2.08
ThO_2-6	120	200	142*	173*	2.09
ThO_2-7	151	RT	55	70	2.18
ThO_2-8	117	RT	140	170	2.22

3.2.2 Uranium samples

As described earlier [Sei07] the UO_2 thin film properties show a more significant dependence on the deposition parameters. The composition is depending on the O_2 pressure and the substrate temperature. With increasing O_2 pressure the composition of the film varies from U_{metal} through U_{metal}/UO_{2-x} mixtures up to UO_2 and ends up with UO_{2+x} [Mis01]. For an O_2 pressure in saturation to produce the higher oxide UO_{2+x} at room temperature also the sub-

strate temperature influences the composition of the film. Temperatures around 300 °C lead to a stoichiometric UO_2 film. As example the XPS spectra (U-4f and O-1s) and UV excited photoemission spectra (VB) for exemplary UO_2 thin films are shown in Figure 6.

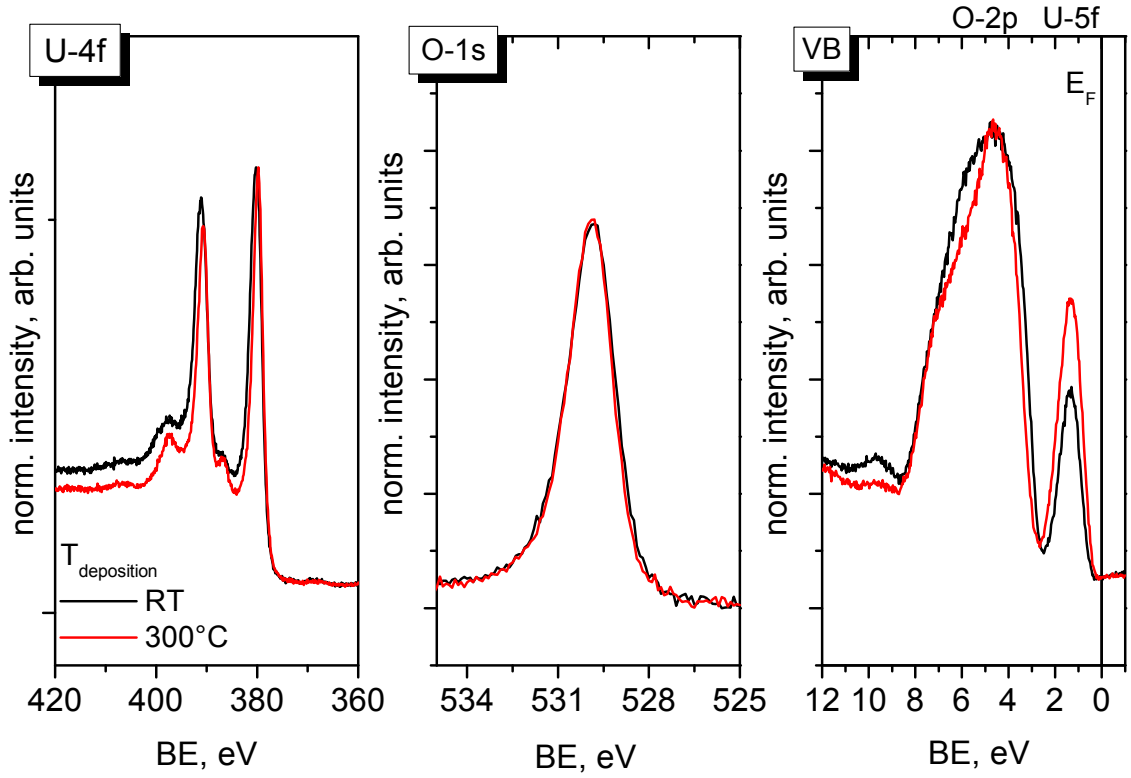

Figure 6: XPS and UPS spectra for UO_2 thin films produced at different temperature: room temperature (RT) and 300 °C. Excitation source is Al K_α with 1486.6 eV (U-4f, O-1s), resp. He II radiation with 40.8 eV (VB) (E_F = Fermi energy). Spectra are normalised to similar height.

The U-4f line for the 300 °C thin film sample shows the typical shape of stoichiometric UO_2 with the significant satellite structures at ~ 7 eV higher BE than the two main lines ($4f_{7/2}$ and $4f_{5/2}$). For the RT sample these features are decreased, respectively a slight splitting of the higher BE satellite can be distinguished. This is thought to correspond to a hyperstoichiometry of the oxide [Col84]. Indeed this is observed in the valence band spectra where the intensity of the U-5f peak ~ 1-2 eV BE (the well localised $5f^2$ level of the stoichiometric UO_2) is significantly lower for the room temperature sample. The intensity of the 5f peak can be taken as a direct measure for the oxidation state of the uranium. The intensity of the 5f level decreases for the RT sample, corresponding to a further oxidation of U(IV) (removal of valence electrons) to a higher oxidation state. Together with this an increased O-2p signal is observed as well indicating the oxidation (broadened, additional intensity ~ 6 - 7 eV).

The uranium oxide samples (in this study mainly used to test the Raman spectroscopic method), were, due to time constraints, not characterised by photoemission anymore. Only the composition (O/U ratio) directly after production was determined by photoemission. Anyhow the oxidation of the surface due to storage under ambient laboratory atmosphere can be followed by XPS. Shown in Figure 7 is a typical example of the oxidation of an UO_2 thin film on the gold electrode of a quartz microbalance crystal under ambient laboratory conditions. A similar behaviour is expected for the (up to 2.4 years) aged $UO_{2(+x)}$ samples. The U-4f and O-1s core level spectra directly after production (red curves) and after some days under laboratory atmosphere (blue curves) are plotted together. Both core level peaks (U-4f and $O\text{-}1s_{oxidic}$) are slightly shifted to higher BE after the storage time. The U-4f satellites (~ 7 eV higher in BE than the main peak) typically for UO_2 are strongly decreased and show some structure in case of the stored sample. This was found to be typical for surface oxidation [Col84].

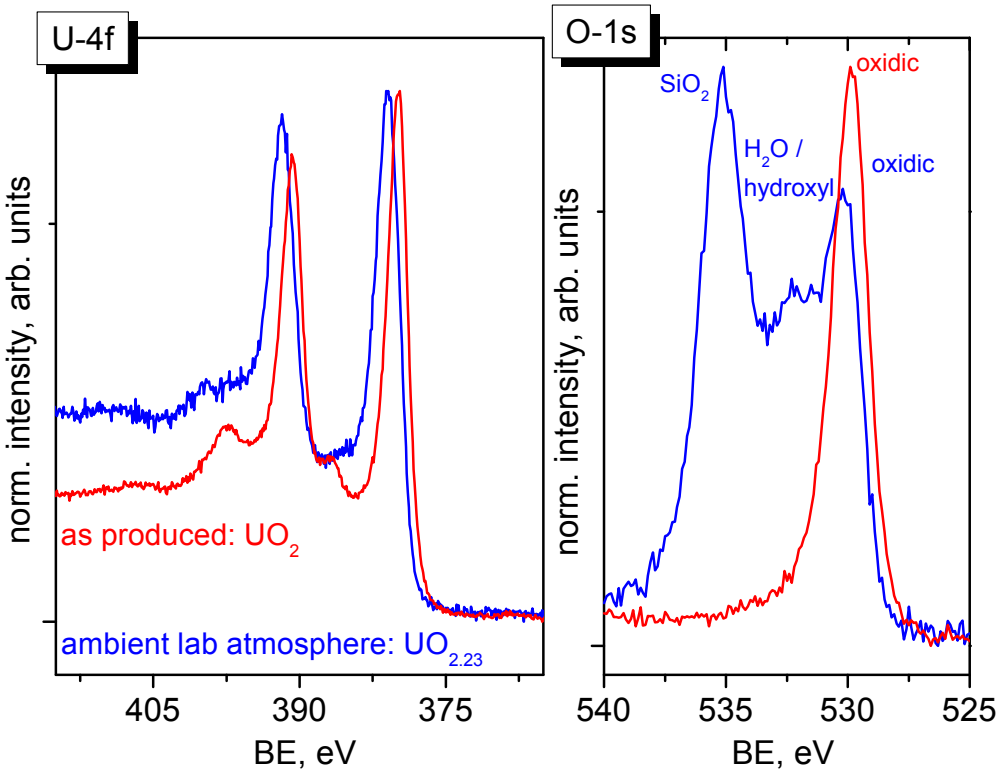

Figure 7: PE spectra (U-4f and O-1s lines) of a UO_2 thin film sample deposited as stoichiometric UO_2 (red spectra) and after several days under laboratory conditions (blue spectra). Excitation source is Al K_α with 1486.6 eV. Spectra are normalised to similar height.

The O-1s peak as well changes its shape due to the storage. Additional to the oxidic peak at BE ~ 530 eV a peak around ~ 532 eV is clearly evolving which is ascribed to water or hydroxyl species at the surface. The peak at ~ 535 eV belongs to the oxidic O-1s signal of the quartz crystal (SiO_2), which is seen in this measurement geometry (larger measuring area).

3.3 AFM

3.3.1 General considerations

Images measured with an atomic force microscope are always a convolution of probe geometry and the sample features that are imaged. Therefore it seems worth to spend some consideration on possible artefacts in the AFM images. The microstructure of thin films (especially under the sputter deposition technique conditions used here) tends to be columnar (Zone 1 or Zone T in the structure zone model [Tho77]) and therewith probably consists of surface structure elements in the size range of a conventional AFM tip. In Scanning Electron Microscopy (SEM) images of UO_2 thin films [Sei06], indeed surfaces defined by small crystallites with size around 100 nm are observed for this sort of sample.

If a surface shows a microstructure with features as sharp as, or sharper than the AFM tip, the picture does not resemble the real microstructure of the surface but is an image of the tip ("tip artefact") [All92, Wes93, Grü92]. This is then, for our thin films, an intrinsic problem which is not necessarily due to some imperfections of the tip (like pyramidal structures or otherwise chipped tips). Anyhow the deviations from the real structure induced by these artefacts would be somewhat easier to detect as the artefact of a spherical tip on a thin film surface with "sharper" features than the tip radius, because in the latter case the observed image may appear very similar to the expected columnar thin film surface. A quantification of the effect is given here after. When the tip scans over the surface with features sharper than the radius of curvature of the tip, then the radius of curvature of the feature, R_i, in the image approaches the radius of curvature of the tip, R, and the image represents only multiple pictures of the tip. R_i can be estimated from height, h, and width, w, determined from the images by $R_i = \{h^2 + (0.5 \cdot w)^2\} / 2h$. In [Wes93] it is shown that, if the radius of a feature is greater than twice the tip radius, the surface is resembled relatively accurately. This is normally the case for our thin films. On the other hand it means that radii ~ 40 nm may not be representative for the thin film surface, but even smaller radii may occur, although they are not detectable in the image. Anyhow even if the size of features like nanoparticles is not given correctly (but an image is produced that is too large) the height information from a line profile measurement should be correct. Artefacts introduced by the scanner (as non linear motion or hysteresis effects of the piezoelectric ceramics of the scanner) are tried to be avoided by testing X, Y, Z linearity with a test pattern. After the measurement typically a "flattening" of the image is done with the data evaluation program WSxM 4.0 [Hor07] to correct for the curved motion of the piezoelectric scanner over the sample surface. Other image processing is avoided, because it may itself introduce artefacts.

3.3.2 Measurements in contact mode

3.3.2.1 AFM measurements on ThO_2 thin films

As for earlier investigations on thin films of UO_2 this mode was used with success, the ThO_2 samples were as well tried to be measured in this mode. Anyhow the quality of the pictures obtained in this mode for the ThO_2 samples was not acceptable for all samples. Figure 8 summarises some of the resulting AFM pictures in contact mode for ThO_2 samples, which are representative for the problems during the measurements. There may be several rea-

sons for the problematic measurements of the ThO_2 samples in contact mode. Firstly, it may be possible, that due to the storage over several weeks the sample surface accumulated some contamination (from laboratory atmosphere, casing, etc.) which is now disturbing the tip scans over the surface leading to the streak marks seen in Figure 8 B. Additionally, in this picture some continuously repeating patterns are observed that are not expected as structural element on the thin film. This distortion of an expected more symmetric feature was observed several times even for images with better quality as seen in Figure 8 A. This was not distinctly seen in the earlier study with UO_2 thin films [Sei07] where the contact mode measurements worked properly and the sample treatment / storage was more or less identical. As well for old UO_2 samples stored for several months under similar conditions as the few weeks old ThO_2 samples shown in Figure 8 similar problems did not occur.

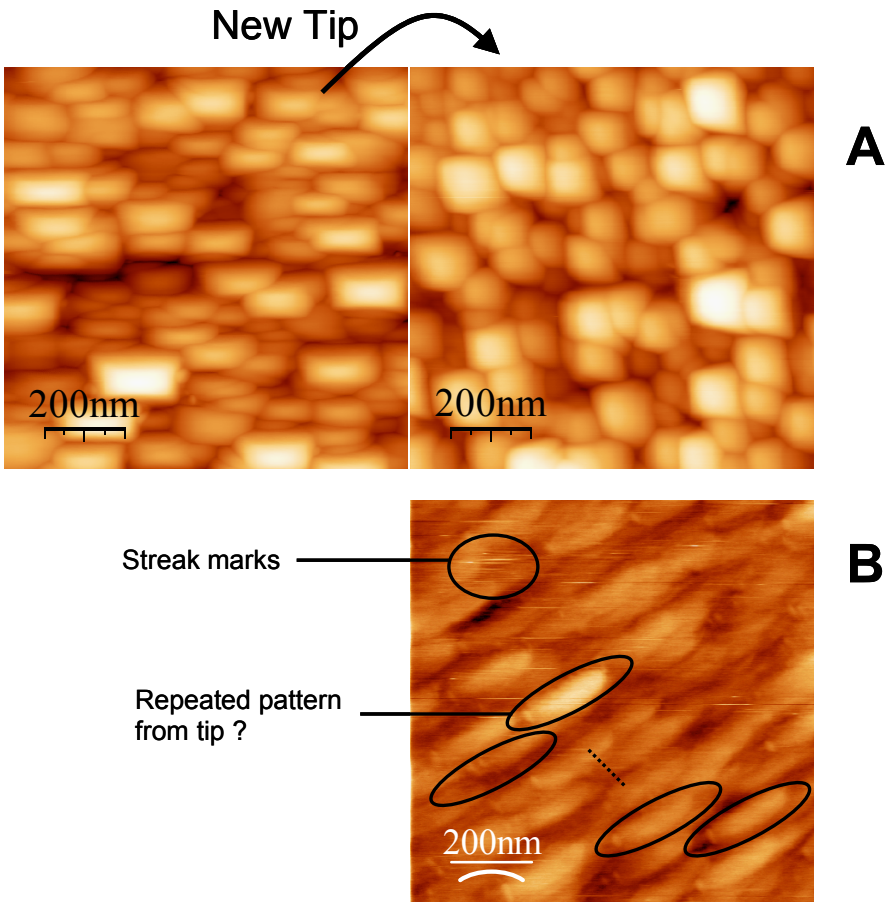

Figure 8: AFM pictures of ThO_2 samples measured in contact mode. The selected pictures show some of the typical artefacts observed. **A**: artefact from tip: after replacement of the tip the structures are more symmetric (as expected). **B**: possibly contaminated surface and tip or charging artefact (marked with the ellipsoids).

Therefore the effect may be intrinsic for the ThO_2. In case of the ThO_2 films we deal with an insulating material (instead of the semiconducting $UO_{2(+x)}$ phases) and scanning the tip (as well insulating) over this surface can probably induce some charging. This seems not a very common artefact, but is reported e.g. for thicker SiO_2 layers on Si [Eme94]. In this paper similar structures are described for high magnifications and / or slow scanning speeds investigating dry, highly insulating materials. Therefore additional measurements were conducted

in tapping mode where the direct contact between tip and sample is limited (see chapter 3.3.3).

3.3.2.2 AFM measurements on UO_2 thin films

Indeed the AFM pictures for the UO_2 depositions on the SiO_2 glass (see Figure 9) indicate what was already expected from the diffractograms. Both products are homogeneous films with similar crystallite sizes (60 nm to 120 nm), height profiles (maximum heights ~ 35 nm) and analog roughness values (6.59 to 6.82 from the 1x1 μm scans). Roughness is given as rms roughness, the root mean square average of the absolute values of the height over a given surface area. In this case (different to the depositions on the Au-electrodes) no particular difference in orientation or morphology is obtained for UO_2 thin films for the different deposition temperatures.

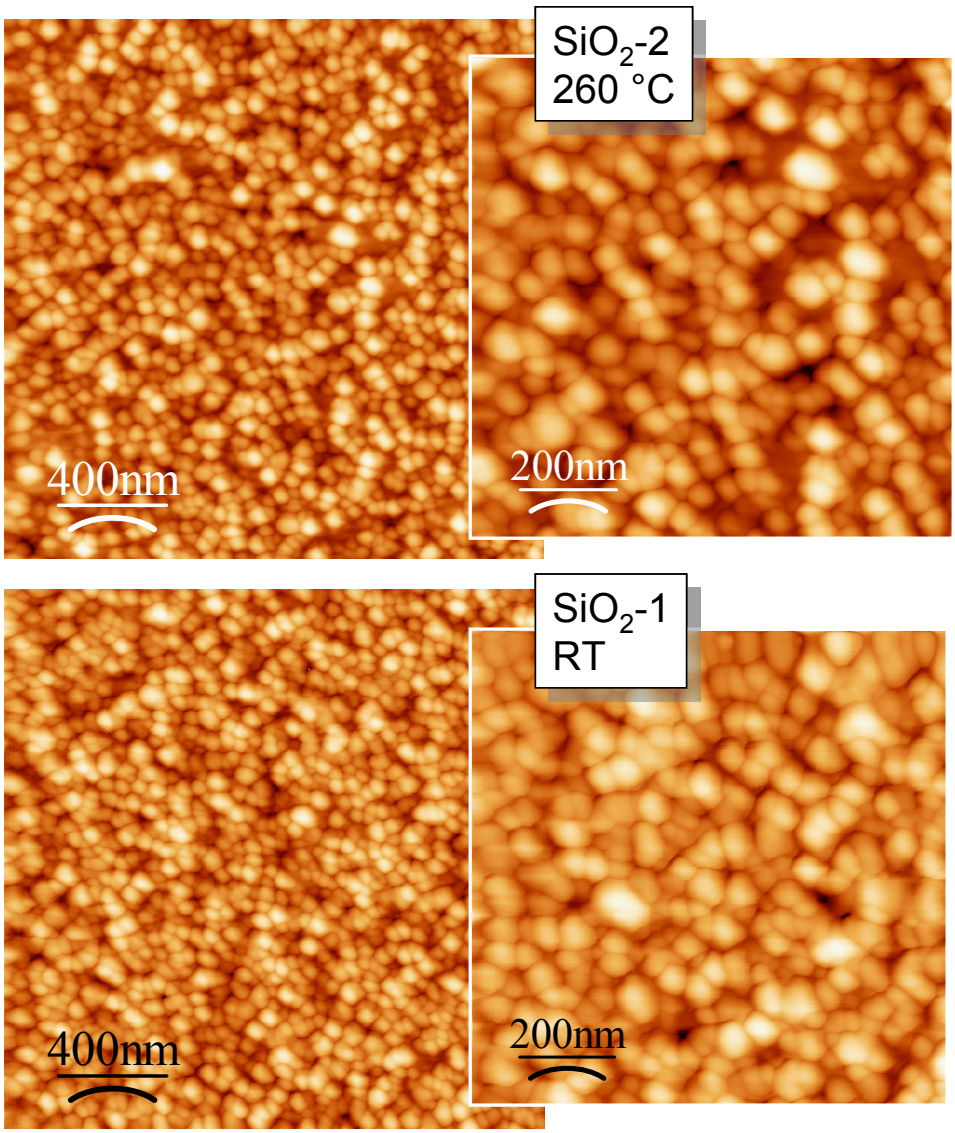

Figure 9: AFM pictures of UO_{2+x} samples on SiO_2 glass substrates measured in contact mode.

Figure 10 shows a comparison of similar surfaces measured either with contact mode or tapping mode AFM. The depositions on the Au-electrodes of the SiO_2 piezocrystals show a similar morphology as expected for the room temperature depositions on this kind of smooth substrate: small crystallite sizes, with relative low roughness. Values for the crystallite sizes are 60 -90 nm for cr 50 and 60 -120 nm for cr1 old. The according rms roughness values for a 500 nm x 500 nm areas are 6.4 and 5.3.

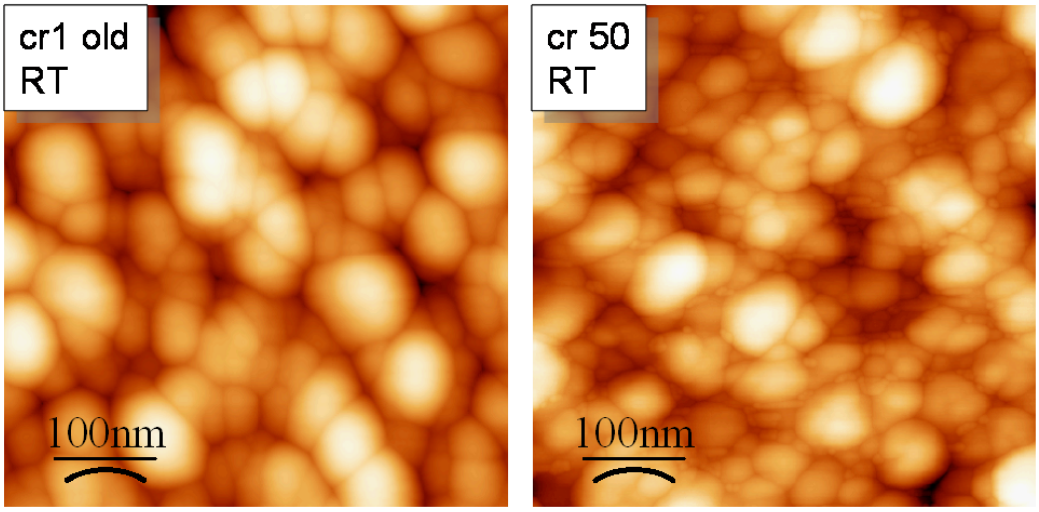

Figure 10: AFM pictures of UO_{2+x} samples on Au substrates (SiO_2 piezocrystal electrodes) measured in contact mode (cr1 old) or in tapping mode (cr 50). Both images were flattened (with a parabolic background subtraction) and a tip surface dilation was run with appropriate tip radius.

In the tapping mode image (cr 50) beside the 60 to 90 nm crystallites also smaller sized structures can be detected. It is not completely clear if this is a real feature of the surface or maybe an artefact from the measurement method (see as well discussion below on the ThO_2 films, 3.3.3)

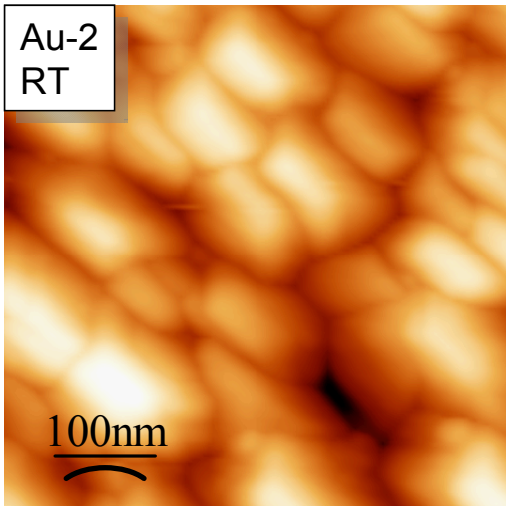

Figure 11: AFM image of a UO_{2+x} sample on an Au plate measured in contact mode (Au-2).

The AFM image of a deposited film on an Au plate with relative rough surface is shown in Figure 11. With these substrates much more structured films with slightly increased crystallite sizes are obtained. This is probably not an effect of the film thickness which is relatively high in these cases (because these films are used for a special application) but indeed of the substrate structure: the film thicknesses of cr 50 (Figure 10) and Au-2 are comparable. The rms surface roughness for the latter film is determined to a value of 17.8. Crystallite sizes are ~ 100 nm and maximum height values are around 100 nm as well. For the films on these substrates also a different orientation in the XRD measurements was observed (see chapter 3.1.2).

3.3.3 Measurements in tapping mode

Additional measurements, mainly of the ThO_2 samples, were conducted in tapping mode to characterise the thin film morphology for these samples before and after the corrosion experiments. As well here in this first test series variations in the images are observed that are assumed to be artefacts or effects of the measurement method. Figure 12 compares images of the same sample in the two modes. The contact mode image (Figure 12, left picture) shows a topography of the thin film surface comparable to the results obtained for UO_2 thin film surfaces. Small crystallites (size range 60 – 120 nm) building up a smooth surface (thin film deposited on a SiO_2 glass substrate) with a rms roughness of 3.84.

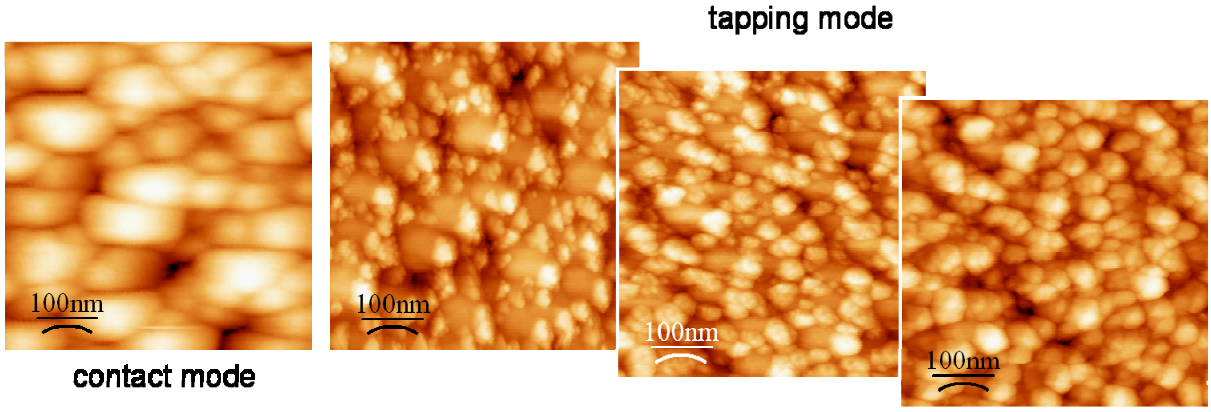

Figure 12: AFM images of a ThO_2 thin film surface (ThO_2-2) measured in contact (left picture) and tapping mode (three pictures on the right). The tapping mode images show an increasing number of scans on the same surface area.

The maximum height values are ~ 25 nm. For the tapping mode experiment a change in the surface morphology is observed with increasing scans over the same surface area. Whereas the early scan (Figure 12, second picture from left) shows a morphology that looks as some bigger crystallites (~ 100 nm) are partly buried under smaller structures (~ 30 nm) the following scans (following images to the right) run into a topographic image resembling a homogeneous distribution of 50 – 70 nm structures. The determined rms roughnesses and maximum heights are similar for all three images (roughness 4.48 – 4.95, $height_{max}$ ~ 33 nm). The varying topography may be explained by the possibility of some tip damage during the measurement or an adhesion of particles at the tip surface. At that point it is not clear, what is the "real topography" of the thin film surface. The above described effect is not necessarily seen for all Th samples, some indeed do not show a variation of the topology with increasing scan

numbers. But a similar structure as seen for the above described sample in the most right picture is observed for other room temperature samples. The following images were taken to compare the samples with different deposition conditions: room temperature vs. increased temperature (Figure 13) and medium deposition rate vs. low deposition rate. Additionally some measurements are done after the corrosion experiments described in chapter 3.5.

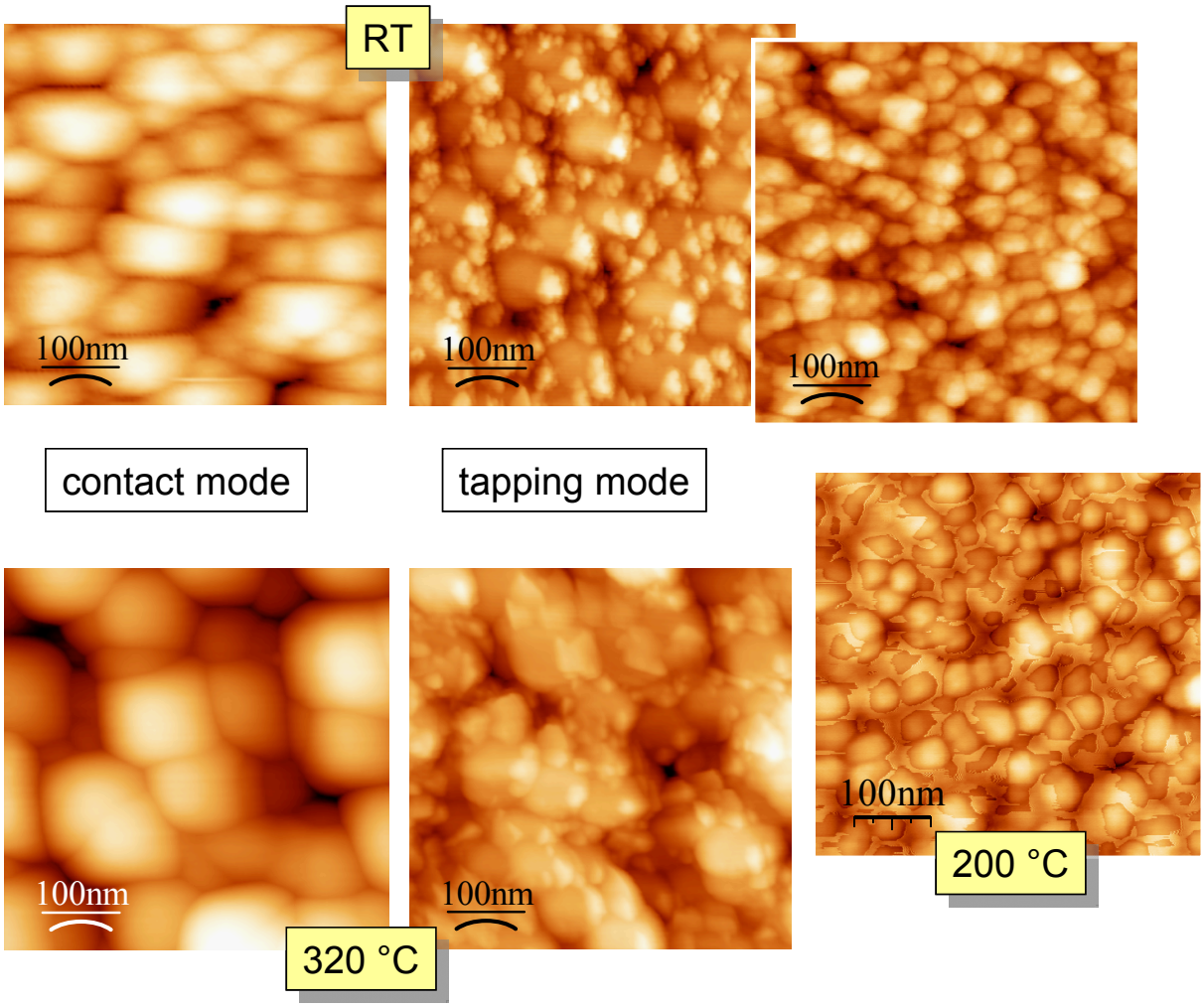

Figure 13: AFM images of ThO_2 samples at different deposition temperatures: room temperature, RT (ThO_2-2), 200 °C (ThO_2-6) and 320 °C (ThO_2-4). For RT and 320 °C images from contact mode measurements and tapping mode measurements are given. All pictures are from the original sample surfaces (before corrosion experiments).

A slight increase in crystallite size may be observed between RT depositions and 320 °C depositions while between RT and 200 °C a difference is hardly distingiushed. The 200 °C sample in the tapping mode measurement is obscured by some sort of overlayer. Its origin is not quite clear up to now. It may either be an overlayer due to some contamination or a "measurement artefact" from the tapping mode as sometimes there are some difficulties with the amplitude of the tip that may be smaller than the height of the ubiquitious water films from lab atmosphere on such surfaces, therewith leading to a sticking of the tip in these surface layers. Table 5 summarises the evaluation for all ThO_2 films on SiO_2 glass substrates. An increase in the rms roughness is observed going from room temperature to 320 °C deposi-

tions, as well the maximum height values increase strongly. An influence of the deposition rate (in these samples determining the film thickness) is not significantly seen. Crystallite size and roughness seem to be higher for the thicker films (medium deposition rate).

Table 5: Synopsis of AFM results for ThO_2 films deposited on SiO_2 glass substrates.

sample	Deposition condition: T and deposition rate	rms roughness	$height_{max}$, nm	crystallite size, nm	AFM mode
ThO_2-1	RT, low	2.23	15	~ 50	tapping
ThO_2-2	RT, medium	4.95	34	100 + 30	tapping
		3.84	25	60 - 120	contact
ThO_2-6	200 °C, medium	1.77	12	30 - 60	tapping
ThO_2-3	320 °C, low	Not measured			
ThO_2-4	320 °C, medium	9.81	82	~100	tapping
		10.98	57	~100	contact

Some of these films are used in the solubility experiments described later on and were measured after the experiment again by AFM. These results are described in the solubility chapter (3.5.1).

3.4 Raman microprobe measurements

Raman spectroscopy in its simplest form is not a very sensitive analytical technique. The cross sections for the scattering processes are usually much lower than those for the absorption or emission. Especially for excitation sources in the visible region the fluorescence of the sample or minor impurities can obscure the Raman scattering signal significantly. On the other hand vibrational spectroscopies are useful tools that can give insight into the structure of solids like perturbations in crystalline lattice [Gün96, Lyo98]. Raman spectroscopy is sensitive to the electrical and mechanical properties of the solid materials and two kinds of parameters influence the spectra. Parameters like atomic mass, bond strength, and system geometry (interatomic distances, atomic substitutions) acting on the mechanical part set the peak positions while the parameters acting on the electrical part (charge transfer) like bond covalency, band structure, etc. will influence the intensity of the peaks. Peak shifts are also attributed to stress phenomena as well as defects are considered to contribute to line broadening (for example [Age91]). A considerable advantage of modern Raman spectrometers is the use of laser excitation sources, that can be easily focused to micrometer range. In com-

bination with a computer controlled microscope system the spectrometer can be used for imaging purposes. This allows the qualitative analysis (fingerprinting) of spatially inhomogeneous samples (in the µ-meter range). Especially in the case of uranium a vast amount of data on naturally occurring mineral phases (e.g. [Dow06]) as well as synthetically produced reference materials (see Annex A) exists in literature. Reference spectra for Thorianite and other Th-containing minerals as well as literature on ThO_2 are available [Dow06, Annex A].

With the discovery of the surface-enhanced Raman spectroscopy (SERS) the analysis of samples containing only trace concentrations of the analytes became accessible [Las93, Lyo98]. It was planned to start some test experiments for this technique concerning our thin films.

3.4.1 Testing the depth resolution

As one of our intentions is the measurement of thin layers of secondary phase precipitates on the sample surface the depth resolution of the available Raman microscope was tested with an experimental set-up shown in Figure 14.

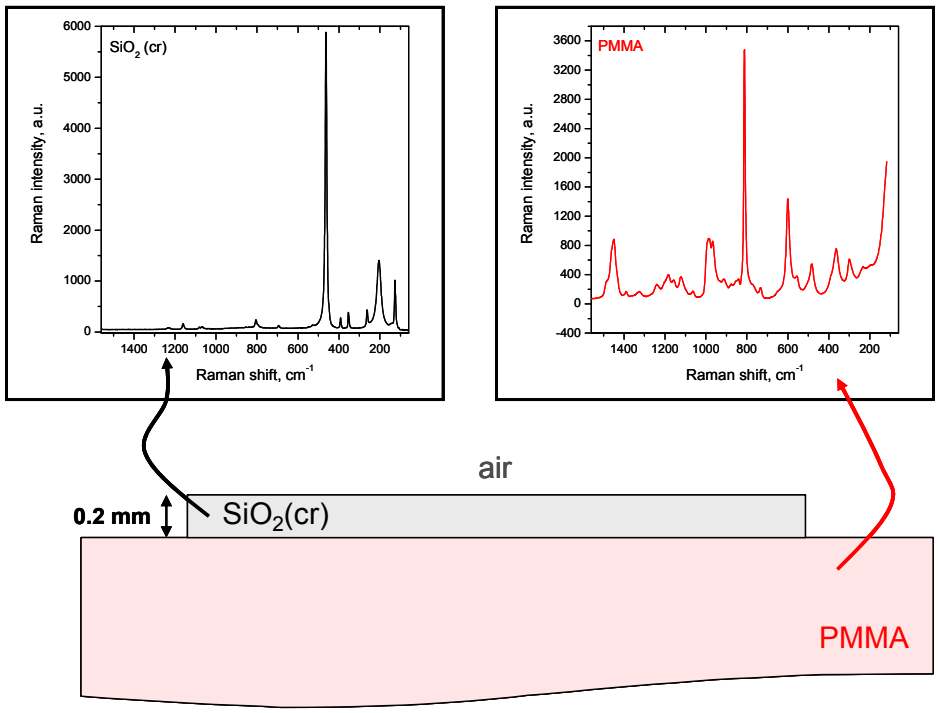

Figure 14: Sample arrangement measured for testing the depth resolution. SiO_2(cr) and the polymethylmethacrylate (PMMA) substrate both show specific Raman spectra (pure spectra shown as insert) that can be deconvoluted.

A quartz crystal of specified thickness is measured on a Plexiglas (polymethylmethacrylate, PMMA) base. The specification for the instrument gives a confocal depth resolution of 2 µm for a 100 x objective. As the available instrument is equipped only with 10 x, 20 x and 50 x microscopic objectives these were tested for their depth resolution with a depth profiling experiment allowed for by the data acquisition system OPUS 6.5. After focusing on the sample

surface, spectra are taken from different depth below the sample surface. This is done automatically by moving the x,y,z-table in z-direction. Figure 15 shows the result for the 50 x objective of the microprobe and the maximum slit size (to be used for the thin film measurements). The profiling was done with 20 steps and a step size of 10 µm, therewith covering nearly the entire height of the SiO_2 crystal.

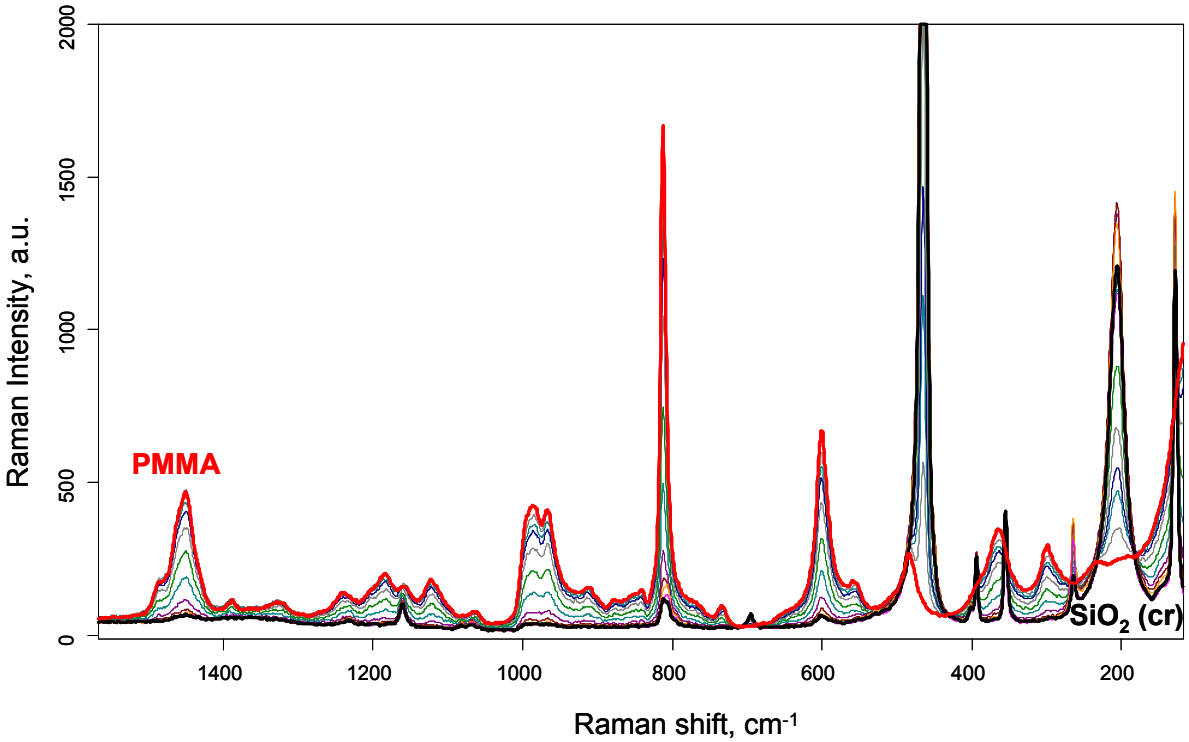

Figure 15: Selected Raman spectra from different depth in the SiO_2 crystal in the sample arrangement shown in Figure 14. Microscopic lens: 50 x, 785 nm excitation wavelength.

It is clearly seen that from a focus depth of -60 µm on a signal from the PMMA base is easily detected. For the 10 x microscopic lens system the resolution is indeed worse: right from the starting point on (focus on the SiO_2 surface) a significant signal for the base PMMA is seen. Results for different lenses and excitation wavelength are given in Figure 16. The relative intensities (determined from the peak areas) of the most isolated peaks for SiO_2 (~280 cm^{-1}) and PMMA (~ 1450 cm^{-1}) are compared for the different depths. It becomes clear that even with the best resolution obtained with the 50 x microscopic lens system for optically penetrable surface layers < 150 µm thickness always the base substrate will be detected as well.

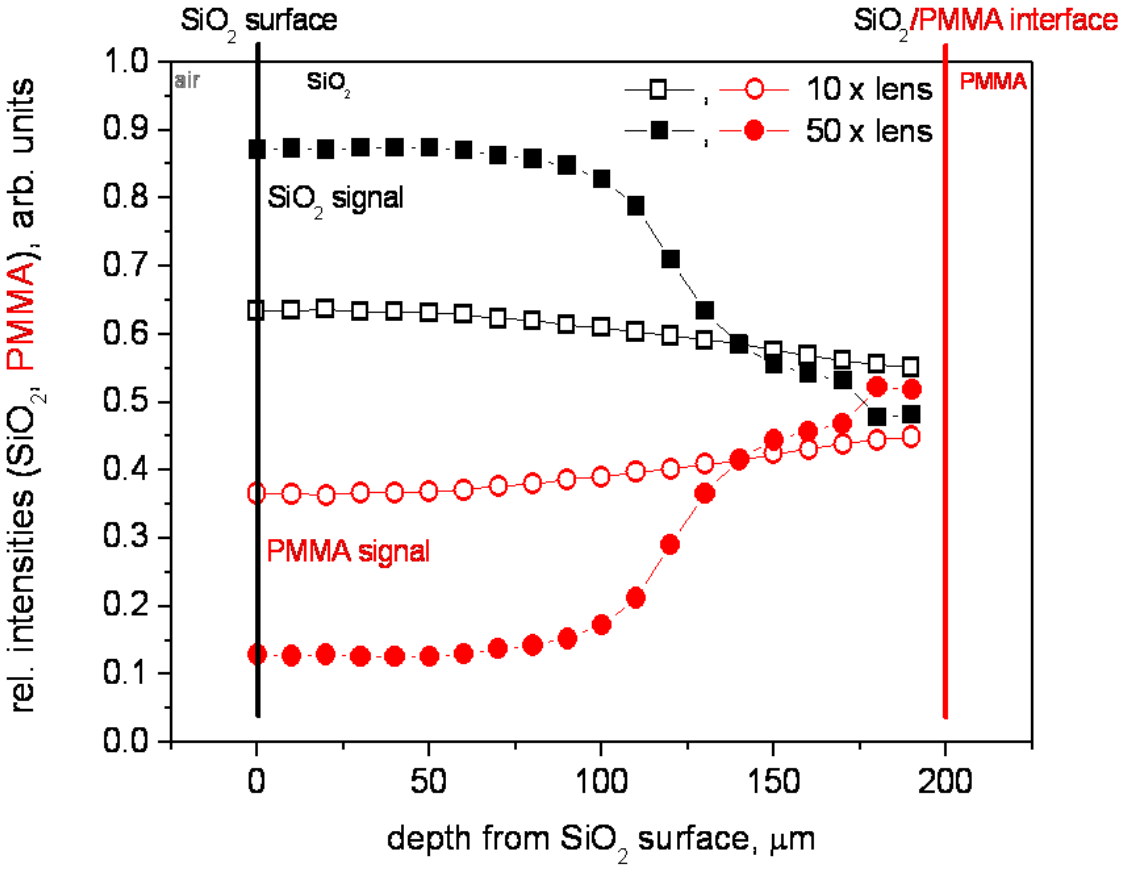

Figure 16: Depth profiling measurements for the sample arrangement shown in Figure 14 for different lenses and excitation wavelength.

3.4.2 Reference spectra from bulk powders

Additionally to the thin film samples (see next chapter) some reference materials are investigated to compare our results from the actual set up to literature data for actinide oxides and compounds. From theoretical consideration it is clear that the actinide dioxides AnO_2 that crystallize in the CaF_2 (fluorite)-type cubic crystal structure should exhibit one Raman active phonon T_{2g} (triply degenerated) with the oxygen ions vibrating in antiphase.

3.4.2.1 Thorium compounds

ThO_2 (cr) and $Th(OH)_4$ (dried and calcined) were measured. The Raman frequencies from literature for the T_{2g} phonon of ThO_2 are summarized in the Annex (Annex A). Our own results are given in Table 6.

A comparison of the three Th compounds measured with the two available excitation sources is shown in Figure 17. The ThO_2 Raman spectrum (Reference A) obtained with 532 nm excitation wavelength appear as expected (Fig. 17-1, blue spectrum): one peak at 465 cm^{-1}. In

the 785 nm excited spectrum (red curve) additional peaks are observed ~ 700 cm^{-1} and in the range 1000 cm^{-1} to 1600 cm^{-1}. There could be several reasons for this observation. The explanation that the peaks intrinsically belong to the Raman scattering of ThO_2 is excluded as this would not correspond to the theoretical background where according to a degenerated T_{2g} phonon only one Raman signal is expected. And this is what we obtained with the 532 nm laser excitation.

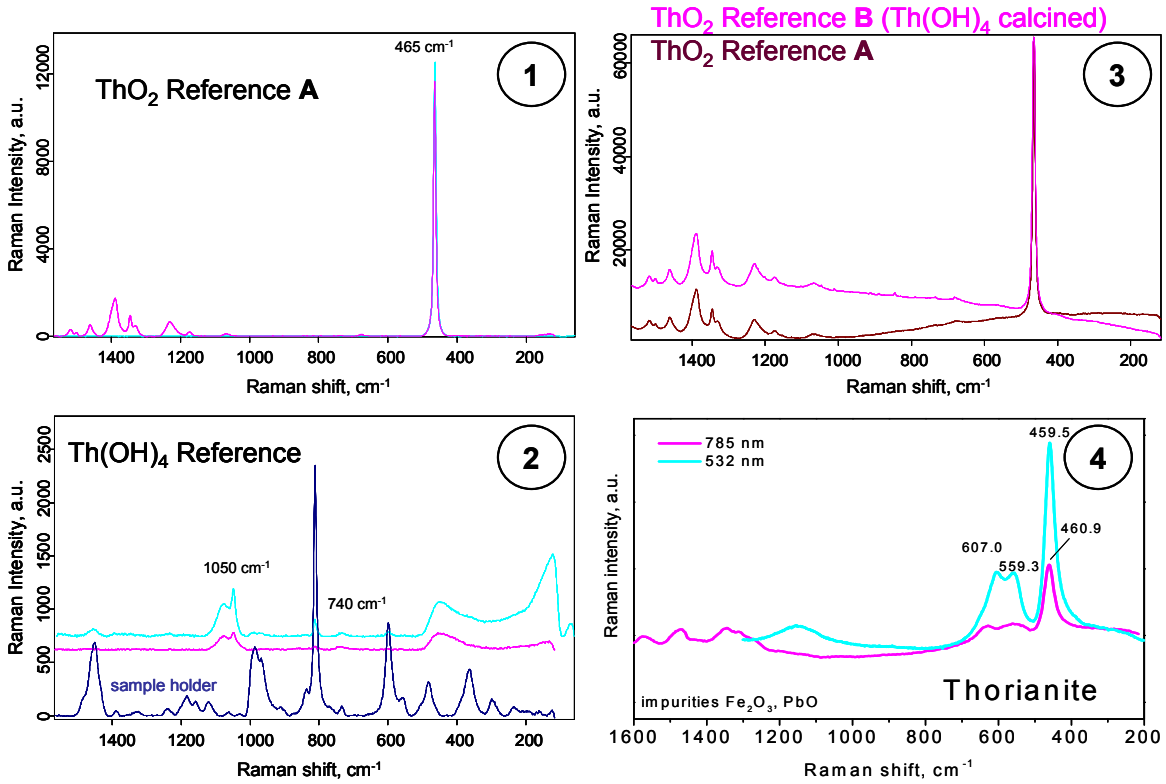

Figure 17: Raman spectra for the Th reference compounds: ThO_2 (plot 1 and 3), $Th(OH)_4$ (am) (plot 2). Excitation wavelengths are 785 nm (red spectra) and 532 nm (blue spectra). For the $Th(OH)_4$ reference as well the Raman spectrum of the sample holder (a PMMA cuvette) is given. Some of the peaks observed in the spectra of $Th(OH)_4$ belong to the sample holder. Thorianite spectra from the RUFF database [Dow06] are given for comparison (plot 4).

So the difference is between the two excitation wavelengths, where the 785 nm excitation eventually can excite transitions other than the Raman scattering mode alone (e.g. electronic excitation with fluorescence) which the 532 nm excitation does not. Still the question is, are these transitions intrinsic to the Th or do we deal with an impurity effect ? For example 3d metals (like chromium) or the lanthanides can produce strong fluorescence signals. Therefore a second ThO_2 sample (B) was produced from another starting material ($Th(OH)_4$ precipitated from Th-nitrate solution). As well Raman spectra of the dried $Th(OH)_4$ were taken (Fig.17-2). For this dried sample no significant differences in the spectra are observed for the

two excitation wavelengths. Beside a very broad peak around 448 cm^{-1} additional peaks are observed. These additional peaks (~ 740 cm^{-1} and the double peak structure ~ 1050 cm^{-1}) are thought to be due to some nitrate that is still left in the precipitated and washed compound. Whereas some other signals (~ 800 cm^{-1} and ~ 1450 cm^{-1}) are easily identified as belonging to the sample holder made from PMMA (for comparison this "blank" spectrum of the sample holder is given as well). After calcination at ~ 1100 °C for several hours, the sample was measured again with the 785 nm excitation and exactly the same spectral features are obtained as for the ThO_2 sample (A) (see Fig. 17-3). Therefore it is concluded that these additional peaks are inherent to the crystalline Th compound. It may be due to a chemically similar impurity that is not eliminated by the reprecipitation process leading to sample (B), and neither any steps leading to the starting material (Th-nitrate). One may think of other tetravalent impurities like Zr or Hf. On the other hand it is only seen in the crystallised specimens and not in the amorphous $Th(OH)_4$ precipitate (which probably makes the fluorescence interpretation less reasonable). Indeed the thin film samples do not show these additional features (see below 3.4.3.2) which can be due to a very pure ThO_2 that is produced from the sputter technique and therewith from metallic Th. Even the signal for the ThO_2 peak itself is quite low so the amount of a minor impurity may be below the detection limit. On the other hand taking into account the nanocrystallinity of the thin film samples this may also reduce the features under discussion as seen for the amorphous $Th(OH)_4$. Additional peaks in the 785 nm excitation spectra are also significantly observed for the Thorianite literature spectra [Dow06] we refer to in Fig. 17-4 (see also Annex Table 11 for further literature data). As this is a mineral sample, impurities are expected and PbO (< 2 %) and Fe_2O_3 (~0.3 %) are given as additional phases for this sample. Anyhow these peaks do not compare to the peaks in our reference spectra.

Table 6: Raman frequencies for Th compounds from this study.

sample	sample preparation	T_{2g}, cm^{-1}	Excitation wavelength, nm	Reference
ThO_2	Thin film (Au substrate)	458	785, 532	This work
ThO_2 (**A**)	Polycrystalline, 99.99 % (Aldrich)	465 + some intensity in the range 1100 – 1600 cm^{-1}	785, 532	This work
$Th(OH)_4$	amorphous, precipitated from $Th(NO_3)_3$ solution, washed NO_3^- free and dried	Very broad peak ~ 448 + add. peaks from NO_3^-	785, 532	This work
ThO_2 (**B**)	$Th(OH)_4$ calcined at 1100 °C	465 + some intensity in the range 1100 – 1600 cm^{-1}	785, 532	This work

3.4.2.2 Uranium Compounds

U_3O_8 (90 %), $UO_3 \cdot xH_2O$, Ca- and Na-uranate were measured as well as thin film samples ($UO_{2(+x)}$). The obtained Raman shifts for these samples are summarised in Table 7. The Raman frequencies from literature for the T_{2g} phonon of UO_2 and other compounds with other vibration modes are summarized in the annex together with our own results (Table 12).

Table 7: Raman frequencies for uranium compounds from this study.

compound	sample form	Raman shift, cm^{-1}	vibration mode	Excitation wavelength,	Reference
UO_2	Thin film	448, 577, 627	T_{2g}	785, 532	This work
U_3O_8	powder	too weak		785, 532	This work
Na-uranate ($Na_2U_2O_7 * H_2O$)	powder	790, 581, 485, 422, 344, 296, 237, 137, 118		785, 532	This work, comparable to [Vol98]
Ca-uranate ($CaU_2O_7 * 3H_2O$)	powder	793, 483, 416, 366, 298, 219, 133		785, 532	This work
Meta-Schoepite ($UO_3 * 2H_2O$)	powder	839, 749 features below 600	U-O stretch	785, 532	This work

For the U_3O_8 sample it was not possible to obtain a Raman spectrum that compares to the spectra from literature. Several sample arrangements were tested, but in all cases no signifi-

cant Raman scattering signal was obtained. This can be mainly due to self-absorption processes in the black coloured sample. Much better results are obtained for the light coloured uranates and metaschoepite samples with colours from light yellow to orange. Spectra are summarised in Figure 18 and Figure 19. For the metaschoepite sample clearly the symmetric U-O stretch vibrational mode is seen ~ 839 cm^{-1}. A double peak structure as reported in [Dow06, Amm02] is not resolved, but a peak ~750 cm^{-1} is seen, which is not obvious in the literature data for schoepite, but reported for γ-UO_3 [Pal00]. Less pronounced features below 600 cm^{-1} compare to the literature spectra of schoepite ($(UO_2)_8O_2(OH)_{12}$*$12H_2O$) in [Dow06].

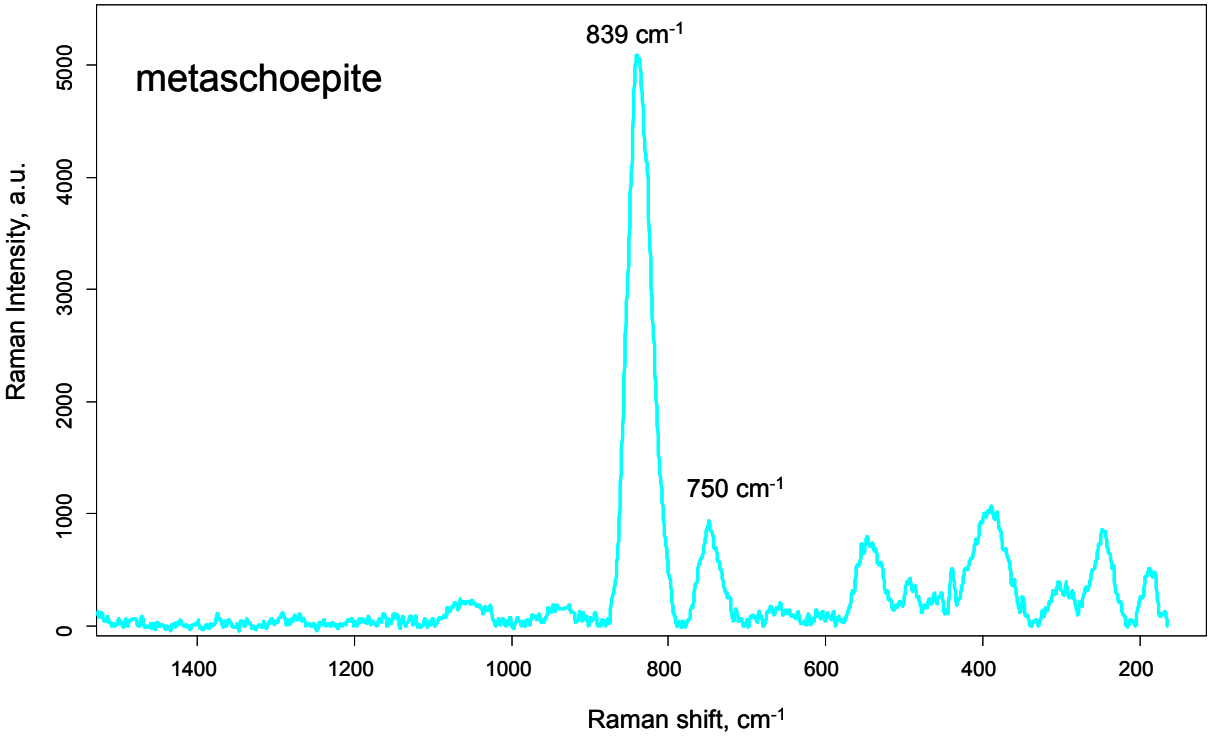

Figure 18: Raman spectra of meta-schoepite reference samples. Excitation wavelength is 532 nm. The 20 x objective of the microscope is used. Background is subtracted ("Gummibandmethode").

The spectra for the two uranates (Figure 19) are very similar what can be expected as they consist of similar structural units. Some conclusions in assignments for the different peaks are reported in literature for sodium uranate [Vol98]. Again for our spectra a peak splitting of the strongest peak ~ 790 cm^{-1} is not resolved. This is as well seen for the Raman spectrum of calciouranoite from [Dow06]. Peak maxima and sample descriptions are summarised in table 12 in annex A.

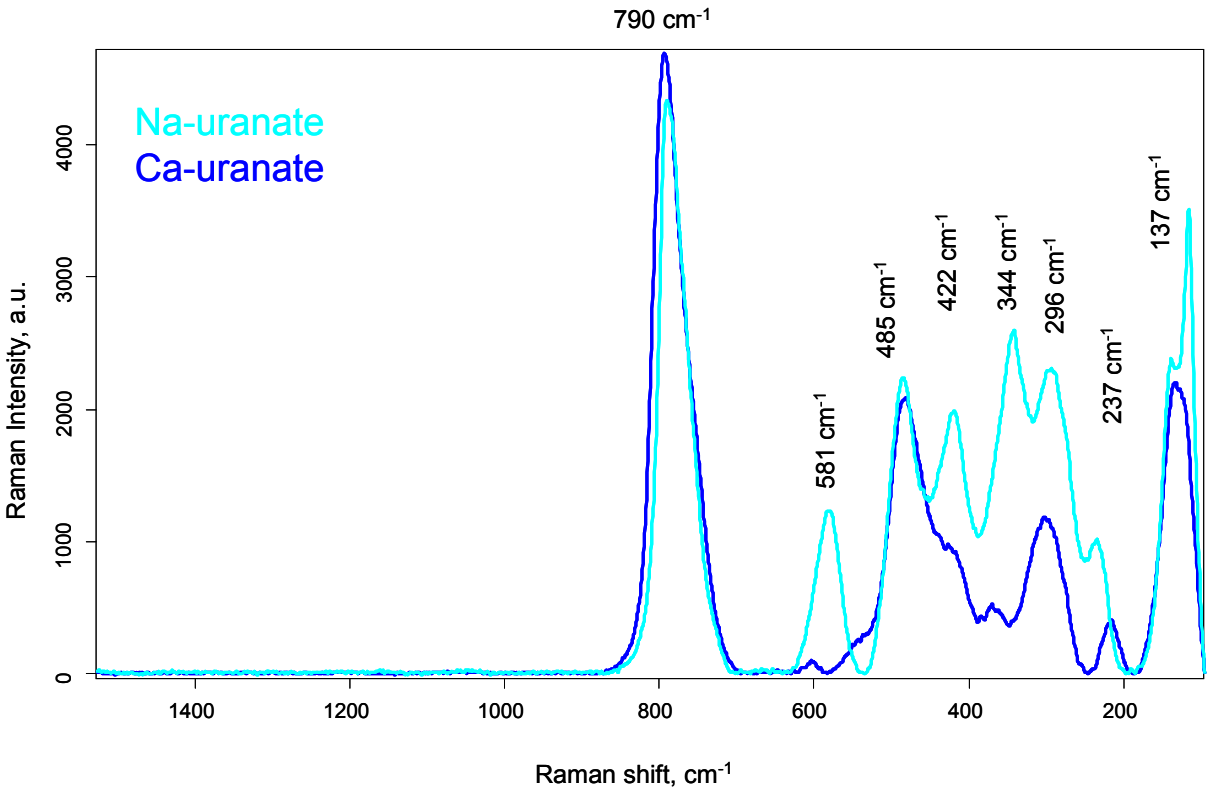

Figure 19: Raman spectra of uranium oxide reference samples: Na- and Ca-Uranate ($Na_2U_2O_7$ *H_2O, CaU_2O_7 *3 H_2O). Excitation wavelength is 532 nm. The 20 x objective of the microscope is used. Background is subtracted (Gummiband-methode").

3.4.3 Thin film samples

3.4.3.1 Uranium dioxide

All measured uranium dioxide thin film samples were deposited on gold substrates. A freshly prepared thin film sample of stoichiometric UO_2 was measured as additional reference (UO_2-1). The obtained Raman spectrum is shown in Figure 20. One peak is observed according to the T_{2g} mode: compared to the literature data (see Annex A) the Raman shift of 448 cm^{-1} is reasonable for $UO_{2.0}$, and in good agreement with the literature data. The two other features around 577 cm^{-1} and 627 cm^{-1} seen in the spectra (for both excitation wavelengths with slightly different intensity ratio) are not assigned yet. They do not belong to the Au substrate (foil) which shows no significant peaks if measured alone. Also for oxidised uranium phases like UO_{2+x}, U_4O_9, U_3O_8 and higher oxides no such features are reported in literature (see Annex A). Only one other UO_2 sample (Au-3) showed a similar pattern (before and after the corrosion experiment in phosphate solution). For some other samples a feature around 630 - 650 cm^{-1} is observed with the 785 nm excitation wavelength, but not the significant peak ~ 577 cm^{-1} seen in the 532 nm excitation Raman spectrum for UO_2-1. An Uraninite spectrum, and also a Thorianite sample, from the RRUFF Raman database indeed showed additional

features between 570 and 630 cm^{-1}. These may belong to some impurities (Fe or Pb) in the minerals. Anyhow such impurities are not expected in the case of our thin films. As the XPS investigations never showed impurities of other heavy metals, this means that the impurity level is below ~ 2 %. If it would be a lower contamination (only detectable by Raman spectroscopy) from the sputter process (e.g. the vacuum chamber or metallic parts other than the actinide sputtered in the plasma) the contamination should be observed also in the ThO_2 samples, which is not the case (see 3.4.3.2). Therefore only a contamination of the uranium metal target may be possible. Also significant amounts of implanted Ar from the sputter gas in the thin films which may lead to defects in the crystalline structure was not detected by XPS.

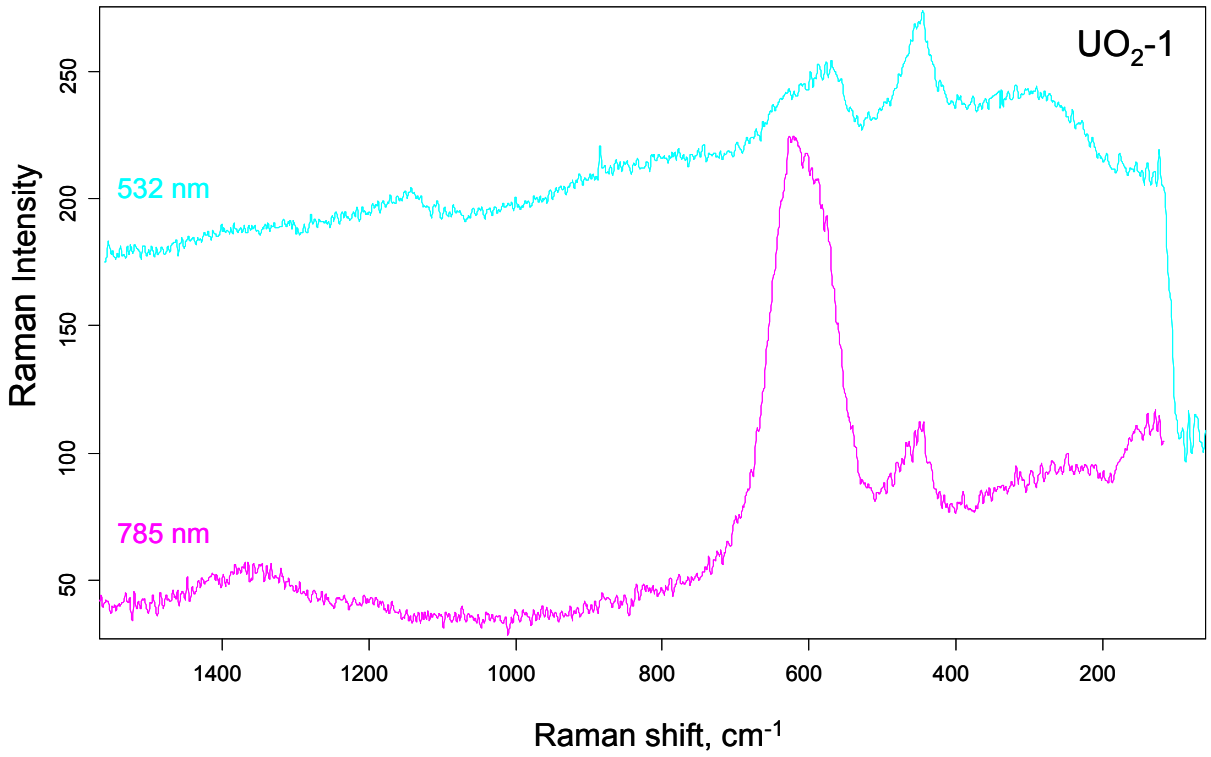

Figure 20: Raman spectrum of a UO_2 thin film on gold substrate. Excitation wavelengths are 785 nm (red spectra) and 532 nm (blue spectra). The 20 x objective of the microscope is used.

The other samples are thin films with an initial $UO_{2(+x)}$ composition that were stored for longer times (up to 2 years) under laboratory atmosphere and are expected to be oxidised up to U_3O_8 [McE98]. For most of the films the Raman signals obtained are quite weak. An increase in the laser power leads to some alteration of the films which indeed can be observed in the microscopic pictures. The area where the incident laser light is focused on the sample surface shows changes in colour and as well the Raman spectrum changes slightly with increasing measuring time. Microscopic picture and corresponding Raman spectra of a UO_{2+x} thin film are shown in Figure 21. The starting measurements (Figure 21, dark cyan) show relative featureless Raman spectra with somewhat obscured features ~ 242 cm^{-1}, 400 cm^{-1}, and 740 cm^{-1}. These may be interpreted as UO_{2+x} features similar to those seen in powder samples [Man03]. For the measurement (with low laser power) in an altered measuring position (marked with the blue circle in the photograph, Figure 21) the spectra given in blue is

obtained. For this position the spectrum is more structured now, with peaks at ~ 242 cm^{-1}, 374 cm^{-1}, 417 cm^{-1} 490 cm^{-1} and 811 cm^{-1}. The overall shape looks comparable to literature spectra reported for α-U_3O_8 [All87, But88]. This would suggest an oxidation of the material in the laser focus. Similar behaviour is observed for iron phases: lower or mixed oxides or oxy-hydroxides were found to undergo degradation to more oxidised phases under high power laser illumination (632.8 nm, 0.7 – 7 mW) [deF97].

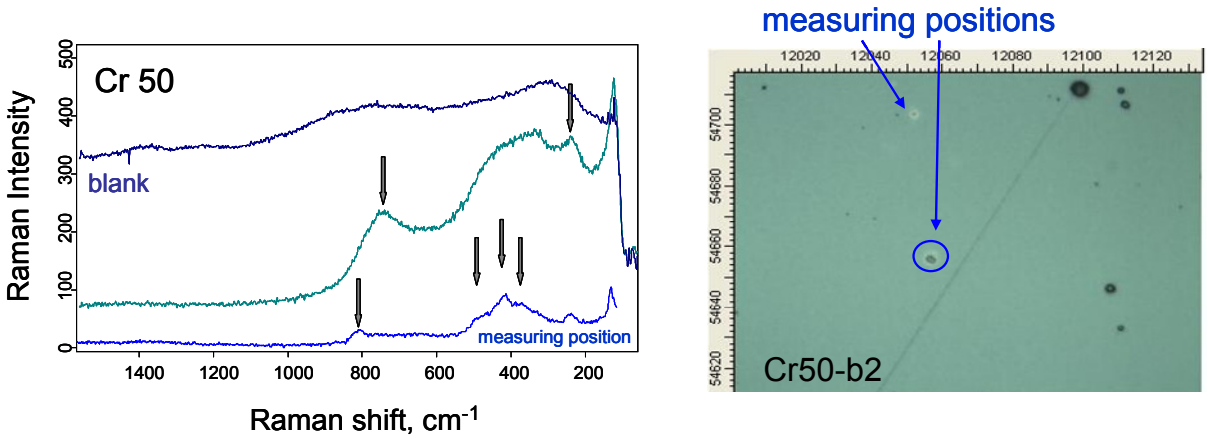

Figure 21: Example for significant alteration of the thin film samples due to incident laser light. Spectra on left side and photograph on the right side were recorded with the 50 x lens system of the microscope. Spectra are measured with 532 nm excitation wavelength.

To obtain Raman spectra from the surface that are as realistic as possible (reflecting the original surface not altered by the laser irradiation) only one spectrum at a certain point of the sample was taken and then the focus was shifted to another (fresh) place for accumulation of spectra. Additionally lowest possible laser power (below 10 mW) was used together with low counting times. Therefore the signal to noise ratio of the spectra is not very good. Anyhow it seems possible to identify different uranium oxide phases in the samples. For sample Au-1 the XRD measurements gave no clear hint on a complete oxidation of the solid (see above), so the Raman investigation supports the interpretation that an oxidised surface layer exists. Spectra obtained with the 532 nm excitation shown in Figure 22 resemble well literature known Raman spectra for U_3O_8 (see Annex A, [All87, But88, Pal00]).

Peak positions (from 532 nm excitation) are 247.5 cm^{-1}, 333 cm^{-1}, 369 cm^{-1}, 420 cm^{-1}, 470 cm^{-1}, 746 cm^{-1}, 797 cm^{-1} (blue arrows). The significant peak in the 785 nm excitation spectrum ~ 637 cm^{-1} is not identified yet (red arrow). In summary this leads to the conclusion that similar corrosion behaviour in air (at RT) is observed for the thin films as for bulk samples [McE98] ending up mainly with U_3O_8. Indeed for one sample (crold1, not shown here) there is a Raman spectrum obtained which seems to show even signals typical for UO_3 phases ~ 742 cm^{-1} and 821 cm^{-1} (like schoepite or γ-UO_3, see discussion above 3.4.2.2).

The thin films prepared on SiO_2 glass gave no results other than spectra of the substrate. The reason may be that these films were of low thickness while the films on gold were somewhat thicker.

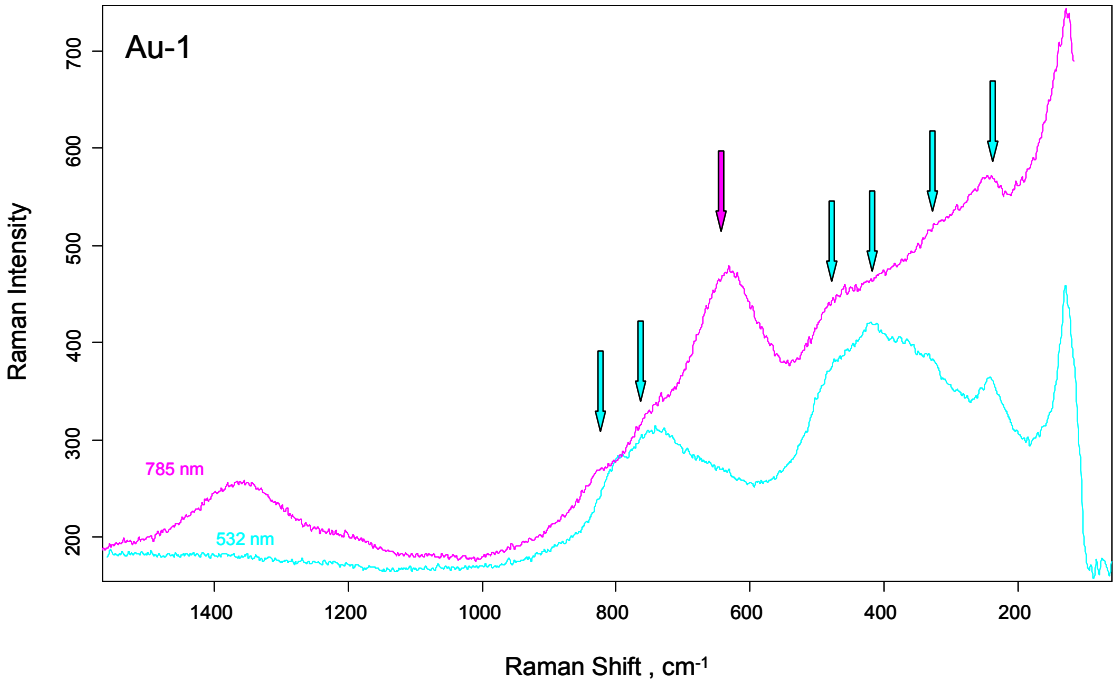

Figure 22: Raman spectrum of an aged UO_2 thin film on gold substrate. Excitation wavelengths are 785 nm (red spectra) and 532 nm (blue spectra). The 50 x objective of the microscope is used.

3.4.3.2 Thorium dioxide

Two different kinds of thin film samples were measured: ThO_2 on SiO_2 glass plates and ThO_2 on the ECQM crystals (the substrate in direct contact with the ThO_2 is gold). For the latter samples the expected Raman peak (T_{2g}) ~ 458 cm^{-1} is seen with low intensity. Typical spectra are given in Figure 23. The somewhat lower Raman shift compared to the bulk powder samples may be explained by the small size of the crystallites forming the film. For the two excitation wavelengths no significant difference is observed in contrary to what was seen for the crystalline ThO_2 reference samples (see discussion in 3.4.2). This may be due to the fact that the hypothesised impurities in the bulk samples are not intrinsic for the production from the sputter process or probably due to the somewhat decreased crystallinity (the sample consists of crystallites in the 100 nm range). Reducing the dimensions of solids down to nanometer scale, confines the electronic and vibrational wavefunctions. On the other hand the surface to volume ratio increases strongly leading to an increased proportion of surface modes that can be observed in nano-sized materials. Such effects may be expected for crystallite sizes smaller than 50 nm and can be described by different models (phonon confine-

ment model, PCM, and elastic sphere model, ESM) [Gou07, Aro07]. But such an approach is not undertaken here.

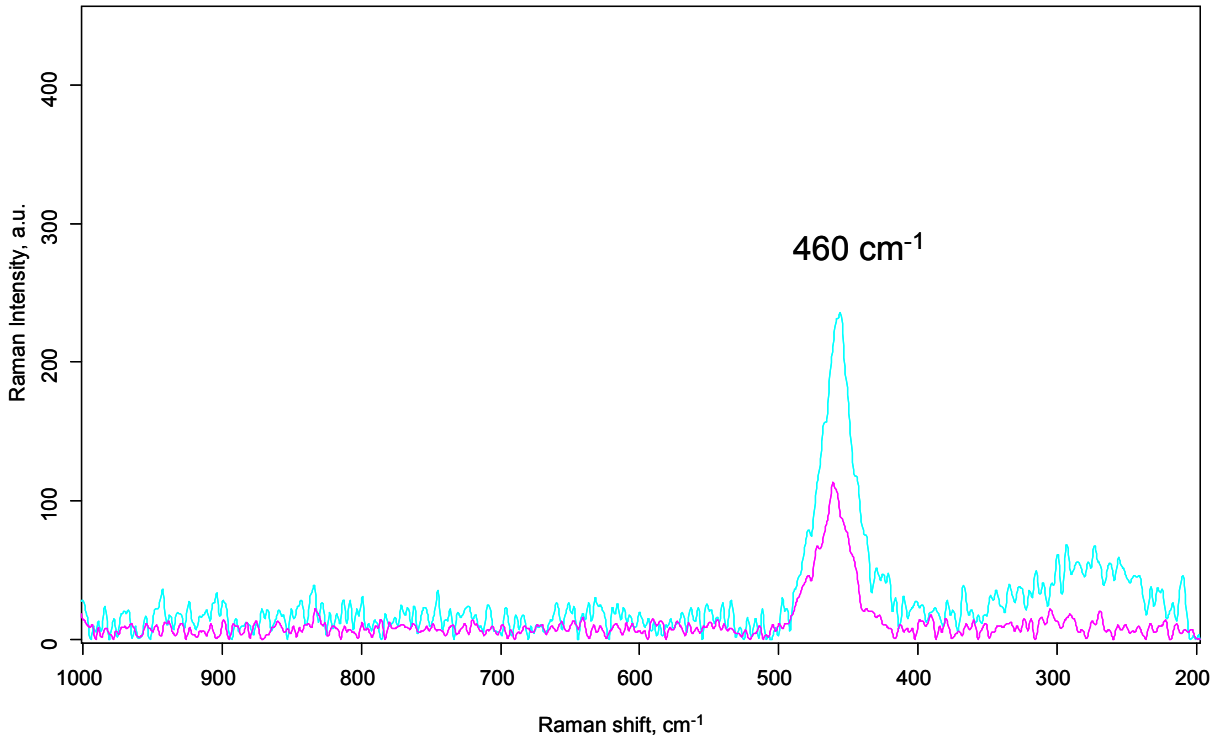

Figure 23: Raman spectra of ThO_2 thin films on Au. Excitation wavelengths are 785 nm (red spectra) and 532 nm (blue spectra). The 50 x objective of the microscope is used. Background is subtracted ("Gummibandmethode").

The samples produced on the SiO_2 glass substrates show somewhat different Raman spectra. One point is that the films are even thinner than the ones described above and another one that the substrate itself exhibits a Raman spectrum which is superimposed with the ThO_2 spectrum in the thin film samples. Only with the thicker samples (ThO_2-2, ThO_2-8 (RT), ThO_2-6 (200 °C) and ThO_2-4 (300 °C)) spectra that are significantly different to the substrate spectra are obtained. Exemplary spectra are shown in Figure 24. Surprisingly here a difference for the two excitation wavelength is found, but it were not the additional peaks observed for the ThO_2 references but different ones: two additional peaks in the range 470 cm^{-1} to 550 cm^{-1} near the expected peak ~ 460 cm^{-1} (which is as well seen) and one other peak at 208 cm^{-1} are observed with the 785 nm excitation. The difference between the two samples produced with different substrate temperature is not very significant, slight differences in the relative intensities for the different peaks (with 785 nm excitation) in the range 450 to 540 cm^{-1} are observed. Table 8 summarises the peak positions for the samples ThO_2 on SiO_2 glass.

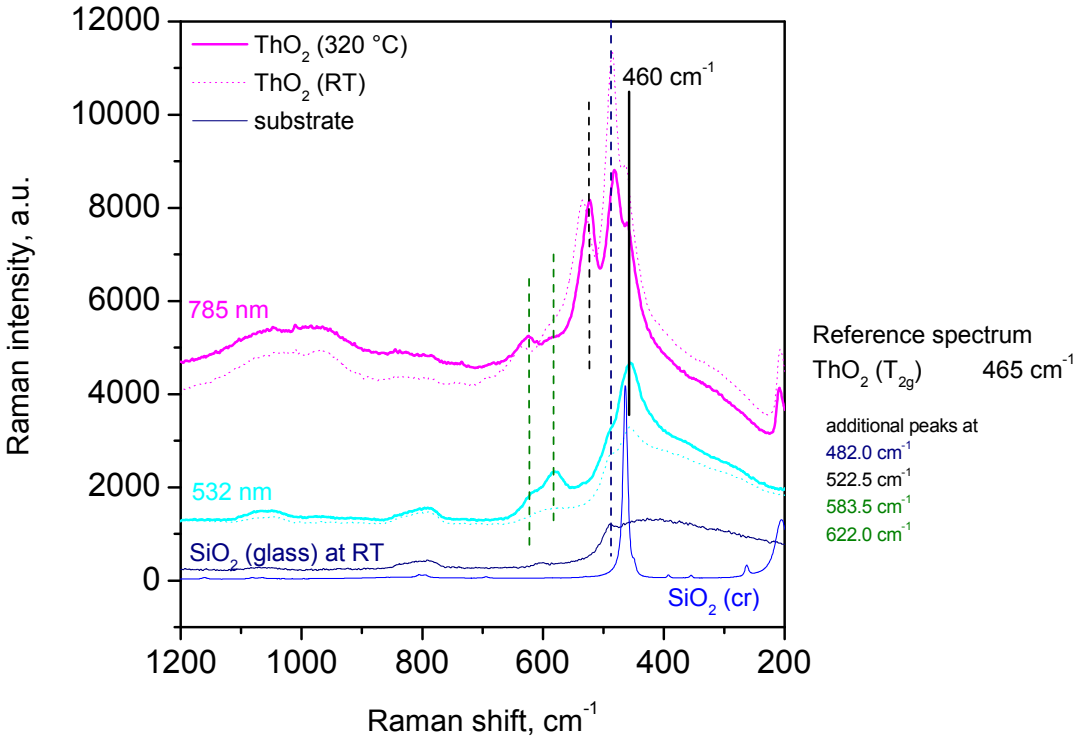

Figure 24: Raman spectra of ThO_2 thin films on SiO_2 glass. Excitation wavelengths are 785 nm (red spectra) and 532 nm (blue spectra). The 50 x objective of the microscope is used. For comparison the Raman spectrum of the blank substrate is given (dark blue) together with the one for a crystalline SiO_2 phase.

It is not clear what the origin of the additional peaks is. For uranium samples in some cases an alteration of the sample due to the irradiation with the laser sources was observed. This was indeed seen in the microscopic pictures as clearly the area of the laser irradiation was detected as darker spot and a different Raman spectrum can be obtained from these areas indicating an oxidation of the sample in the irradiated spot. But such an alteration would not be expected for the ThO_2 samples and no change of the irradiated area in the microscopic pictures was observed. Probably a temperature induced change in the SiO_2 glass substrate due to (pre-)heating of the substrate in the production process may leading to some recrystallisation may account for the 484 cm^{-1} intensity and peaks 1 and 2 but these two should be as well observed for both wavelength as it is seen for the crystalline SiO_2 sample (blue curve). Unfortunately there is no blank test with a heated SiO_2 glass substrate. The additional peaks 4 and 5 (Figure 24, green line marks) are observed for both excitation wavelength and show slightly increased intensity with increasing the production temperature. Anyhow an assignment is not yet possible.

In conclusion it seems that the thin films deposited on gold substrates gave the most reasonable results, while the deposition on SiO_2 glass seems to influence strongly the Raman spectra of the ThO_2 films due to what reason is not clear by now. This effect is not significant for the UO_2 thin films.

Table 8: Synopsis of the Raman shifts for the ThO_2 thin film samples on SiO_2 glass. (sh): shoulder, (w) weak.

sample	Peak 1	Peak 2	T_{2g}*	Peak 3*,a	Peak 4	Peak 5
ThO_2-2 (RT)		208 cm^{-1}	461 cm^{-1}	482 cm^{-1}	536 cm^{-1}	
ThO_2-8 (RT)		205 cm^{-1}	461 cm^{-1}	484 cm^{-1}	526 cm^{-1} (w)	
ThO_2-6 (200°C)	169 cm^{-1}	208 cm^{-1}	455 cm^{-1} (sh)	486 cm^{-1}	531 cm^{-1}	633 cm^{-1}
ThO_2-4 (320°C)	169 cm^{-1}	208 cm^{-1}	464 cm^{-1} (sh)	484 cm^{-1}	523 cm^{-1}	625 cm^{-1}

* Peaks observed in the 532 nm excited Raman spectra. All other peaks are additionally observed in the 785 nm excited spectra. [a] Peak as well seen in the substrate spectrum.

3.4.4 Surface enhanced Raman spectroscopy (SERS)

In this technique the Raman cross-sections for molecules are enhanced by a factor of 10^6 due to their contact with rough metal substrates or small metal particles. The effect was initially observed for analytes in solution binding to the metal surfaces [Lyo98], but also the reverse effect is observed enhancing the Raman scattering from surface species due to a layer of metal nano-particles deposited on the surface for example [Par08, Che06, Hua00, Lop98]. The signal amplification results from the interaction between the electromagnetic field induced by the laser excitation and the surface plasmon of the metal. The effect is theoretically not completely understood up to know. Electromagnetic (EM) or charge-transfer (CT) theories are proposed as explanation. Indeed it seems both mechanisms are operating in practice, but their relative importance may depend on the specific experimental conditions. In the EM model the electric field in metallic nano-particles (or tips sticking out of a rough surface) becomes greatly enhanced if the incident photon energy is in resonance with a normal mode of the conduction electrons of the metal (surface plasmon excitation). If the particle size is smaller than the incident wavelength, the electric field depends only on the dielectric constant of the metal. Therefore Ag, Au and Cu are often used for SERS enhancement as their wavelength dependent dielectric functions produce a maximum electric field in the visible region. This amplified field is additionally (additional to the electric field associated to the radiation) induced to the analytes in the near surroundings of the particle. These molecules or compounds then can scatter enhanced intensity. In the CT model a physi- or chemisorption of the analyte on the metal particles surface is assumed. This allows an electron transfer (via tunnelling or hybridisation) from the metal to the excited electronic level of the analyte and leaves him in a higher vibrational level when the electron is moved back to the metal. Here electron-hole recombination induces a photon emission. The process is resonant when the

energy difference between the excited level in the adsorbed analyte and the Fermi level in the metal is of the order of the incident photon energy.

Metal substrates or particles that are often used for SERS are noble metals (like Ag, Au, Pt, Pd), free-electron like metals (Al, Na, K, etc.) and transition metals (Ni, Cu etc.). Here maximum enhancements are expected in the visible region for the excitation (500 to 700 nm) at least for silver, copper and gold. A few differences between SERS and conventional Raman spectroscopy results are encountered in literature. 1) The vibrational modes in the SER spectra seem to be shifted compared to the conventionally obtained spectra and 2) for measurements in colloid containing solutions the peak width in the SER spectra is increased compared to the width of the peaks obtained with conventional spectroscopy of the corresponding solid materials.

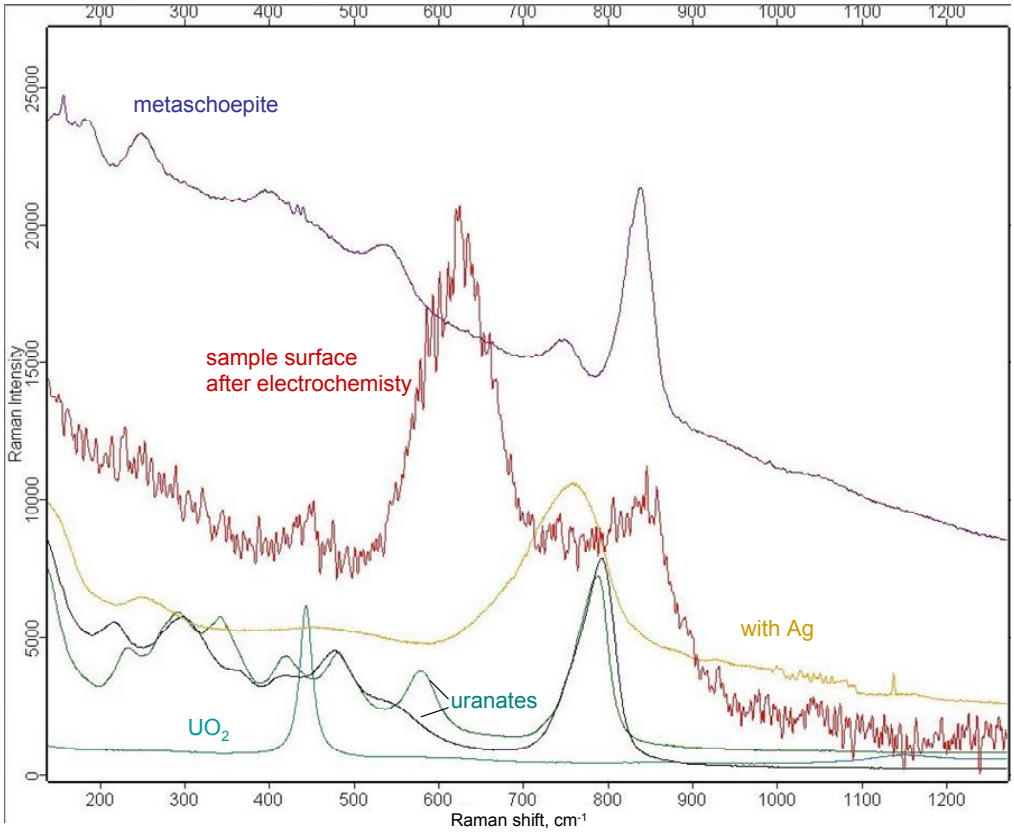

Figure 25: Raman spectrum of an oxidised UO_2 film without (red) and with silver deposition (yellow). For comparison UO_2 (turquoise), UO_3 (violet) and the two Uranate phases (green and black) are given.

Due to some time limitation only very few experiments could be conducted to test different possibilities of the enhancement. A summary of the samples and the preparation procedure is given in table Table 9.

All preparations except the evaporated silver (and gold) failed to enhance the Raman signals of the samples. In case of the silver deposition on an oxidised UO_2 film indeed a different

spectrum is observed after the silver deposition. Figure 25 shows the Raman spectra of this film without (red spectrum) and with the silver layer (yellow spectrum). It is not clear what the observed broad peak (~ 750 cm^{-1}) could be assigned to. It is possibly the shifted uranyl signal usually observed ~ 840 cm^{-1}, or the enhancement of the peak ~ 760cm^{-1}, which was tentatively assigned to a γ-UO_3 phase (together with a peak ~ 845 cm^{-1}).

Table 9: Synopsis of SERS samples and preparation procedure.

sample	metal	procedure
ThO_2	Au evaporation	Evaporated on surface
ThO_2	Au nano-particles*	Au_{coll} solution dried on surface
SiO_2(cr)	Au nano-particles*	Au_{coll} solution dried on surface
UO_{2+x}	Au nano-particles*	Contacted with Au_{coll} solution
UO_x	Ag evaporated	Evaporated on surface

* solution of 20 nm Au colloids

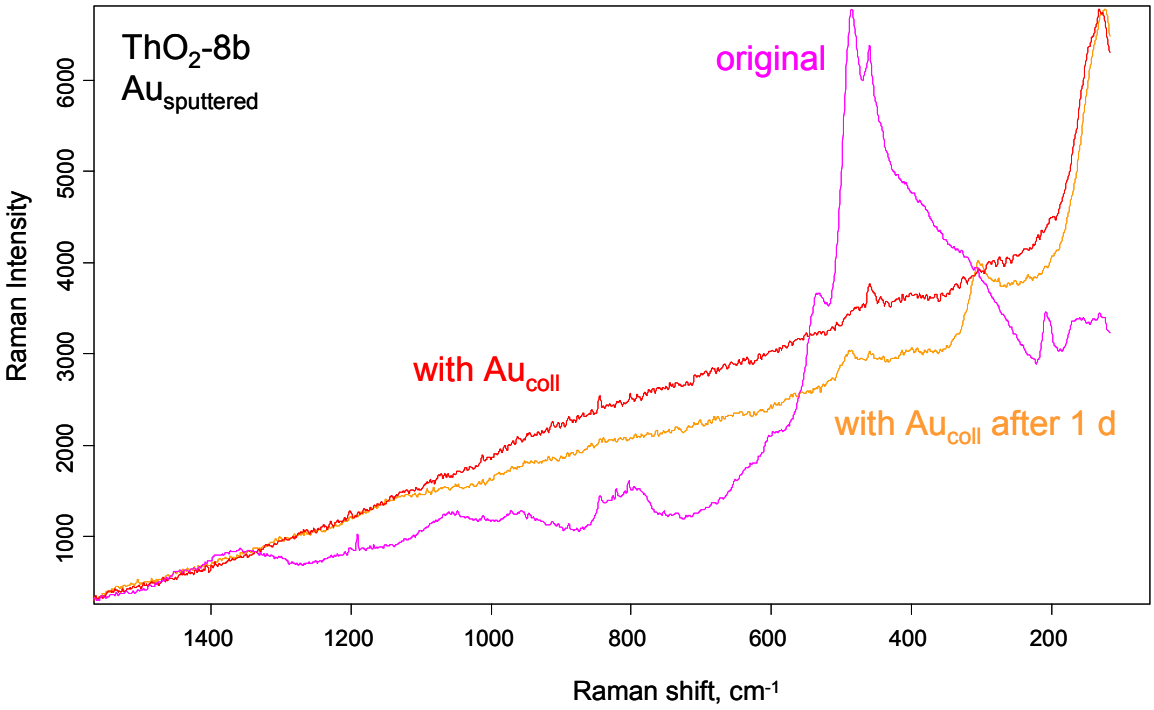

Figure 26: Raman spectra of ThO_2 thin film on SiO_2 glass: original and with sputter deposited Au film. Excitation wavelength is 785 nm. The 50 x objective of the microscope is used.

Figure 26 shows the ThO_2 spectra for the gold evaporation on the surface. It is seen that no enhancement of the signal is obtained but the intensities assumed to belong to the substrate (SiO_2) are reduced leaving behind only the T_{2g} mode of ThO_2 at ~ 458 cm^{-1}. But measuring the same sample the following day a slight change in the spectrum is observed.

To come to a conclusion it seems that using metal substrates or metal evaporations on the surface are the most promising procedures for the Raman measurement of thin films.

3.5 Corrosion / solubility experiments with thin film samples

First results for the solubility of ThO_2 thin films are obtained. Also for UO_2 thin films up to now only short term corrosion experiments with electrochemical techniques are available [Sei06], that are not easily to compare with data from solubility experiments. Owing to time constraints only very limited solubility experiments are achieved. Aqueous solutions of NaCl, phosphate and carbonate are chosen as media for the corrosion, resp. solubility, experiments. The following compositions were prepared: 0.01 M NaCl, a phosphate buffer with a total phosphate concentration of ~ $3.3 \cdot 10^{-4}$ M (background electrolyte is 0.01 M NaCl, I = 0.011 M) and a carbonate solution with a total carbonate concentration of ~ 0.01 M (I = 0.011 M). More detailed information on the preparation and composition is given in chapter 2.1.3. Samples are kept for 18.5 d, resp. 25 days, under the electrolytes. Different vials (glass and PE) are used in the reference experiments with ThO_2(cr) to check for an influence of silicate on the reactions as the substrates used for the thin films mainly are SiO_2 glass or quartz. Si is detected only in few samples above the detection limit ($3.6 \cdot 10^{-5}$ mol/L, calculated for the original solutions). These are the solutions that are kept in glass vials. None of these solutions showed the calculated Si content from SiO_2 (am) or SiO_2 (cr) solubilities probably due to slow dissociation kinetics. Detection limits for uranium and thorium calculated for the original solutions are around 4.2 to $4.3 \cdot 10^{-11}$ mol/L. Owing to a background of uranium in the electrolyte solutions of around $5 \cdot 10^{-10}$ mol/L and a content of uranium detectable in solutions from blank samples (testing vial and substrate leaching) of around $1.5 \cdot 10^{-8}$ mol/L any significant uranium concentration is only above this latter limit.

3.5.1 Thorium

In the experiments with ThO_2 (cr) powder and ThO_2 thin films it is observed that the thin films gave significantly lower thorium concentrations in solution than the bulk samples. The results from these experiments in 0.01 M NaCl, $3.3 \cdot 10^{-4}$ M phosphate buffer and 0.01 M carbonate buffer are summarized in Figure 27. For the static batch experiments with the crystalline, anhydrous ThO_2 15 ml of the buffer solutions are added to an appropriate amount of the powder (to reach a maximum concentration of ~ $5 \cdot 10^{-3}$ M). The samples are stored at 22 ± 2 °C. Thin films on their substrates (~ $1 \cdot 10^{-4}$ M maximum concentration) are immersed in 5 ml of the buffers. Aliquots of the solutions are measured after ~18 days (Figure 27, left graph A) by ICP-MS. No separation procedure (like ultracentrifugation) was applied in this case. While for the thin film samples the thorium concentration in the NaCl and phosphate buffer is below the detection limit and very low ($1.7 \cdot 10^{-10}$ M, resp. $3.0 \cdot 10^{-10}$ M) in the carbonate buffer, the concentrations obtained from the powder samples are significantly higher ($9.7 \cdot 10^{-9}$ M up to $6.5 \cdot 10^{-7}$ M). The Th (aq) concentrations obtained in 0.01 M NaCl are in the range of values from literature for ThO_2 (cr) and ThO_2 (am) (with I = 0.5-0.6 M) summarised in [Nec03,

Nec02] despite the fact that in our case no phase separation by ultracentrifugation is conducted (unseparated values for ThO_2(am) ~ log[Th]= -6.2 ± 0.5 [Nec02] after 211 days). Usually solubility experiments with crystalline ThO_2 in near-neutral (and alkaline) solutions give solubility data that exceed the thermodynamic calculations by orders of magnitudes [Nec03] approaching values for the amorphous solids. This is explained by the dissolution of small amounts of amorphous parts present in the crystalline solid. These are thought to remain as hydrolysed species $(Th_x(OH)_y^{4x-y}$ (aq), monomeric or polynuclear) in solution as a result of an irreversible dissolution reaction of the crystalline ThO_2. The polynuclear species are even not separated by ultracentrifugation. For our results on the thin films this may lead to the conclusion that the amount of this amorphous parts is lower as for the ThO_2 (cr) powder. As the solid mass to solution ratio in the experiments with the thin films is about 1.5 orders of magnitude smaller than for the powder experiment the difference of > 2.7 orders of magnitude in the concentration (between the ultracentrifuged sample and the thin film result (below the detection limit) in phosphate media) indeed seems significant, corroborating the very low content of "amorphous" material in the thin films. An influence of the ThO_2 precursor and the calcination temperature on the ThO_2 solubility in $NaClO_4$ (I = 0.1 M) is described in [Hub01].The Th (aq) concentrations for pH > 5 after 10 days of leaching obtained with high fired ThO_2 (cr) reach the LOD ~ $2.2 \cdot 10^{-10}$ M. This is lower than the values obtained with the amorphous solids / precipitates [summarised in Nec03, Nec02]. Newer investigations try to determine a relationship between surface properties and solubility behaviour for ThO_2 (cr) by using well characterised ThO_2 (cr) spheres and Th-229 spiked solutions to evaluate attachment and detachment processes during solubility experiments [Van08].

For the complexing buffer carbonate an increased solubility can be expected from literature [Alt05, Alt06 and references therein] while no carbonate solids are assumed. For the phosphate case the formation of a secondary phase is not excluded as the phosphate solids are indeed discussed as immobilisation matrices with very low solubility [Dac04, Dac06, Cla06]. Literature data on solubility experiments of the oxides in phosphate media are limited, anyhow in experiments with UO_2, Uranyl-phosphates like Chernikovite $(H_2(UO_2)_2(PO_4)_2 \cdot 8H_2O)$ can be detected as secondary phases [Rey08]. Indeed also Thorium phosphates/diphosphates and Th-monazites are reported as stable mineral phases or synthetic solids [Dow06, Dac04, Cla08]. Compared to the NaCl experiment the aqueous Th concentrations from the phosphate and carbonate experiments are increased for the powder samples. For the thin film samples only the carbonate media leads to an increase in solubility above the detection limit for thorium. For the powder samples in phosphate and carbonate media the ultracentrifugation process (after 25 d) leads to a decrease of the aqueous thorium concentration of about 1.7 orders of magnitude for the phosphate solution and 1.2 orders of magnitude for the carbonate solution compared with the non-centrifuged solutions (Figure 27 B). Indeed for both electrolytes increased Th(aq) concentrations are obtained for the 25 d sampling (without ultracentrifugation) showing that, as expected, the experiments did not reach equilibrium after this experimental period. Anyhow the aqueous Th concentration obtained in the carbonate electrolyte is lower than the value found in literature [Alt06] in $NaHCO_3$-Na_2CO_3-NaCl solutions where for low ionic strength (0.1 M) and 0.02 M C_{tot} the coexistence of the (122) and (114) mixed hydroxide-carbonate complexes is proposed (pH ~ 9.5): log[Th(IV)] ~ -6.2 and log[Th(IV)] ~ -7.2 our value. No calculation for correction to appropriate ionic strength and carbonate concentration were done up to now.

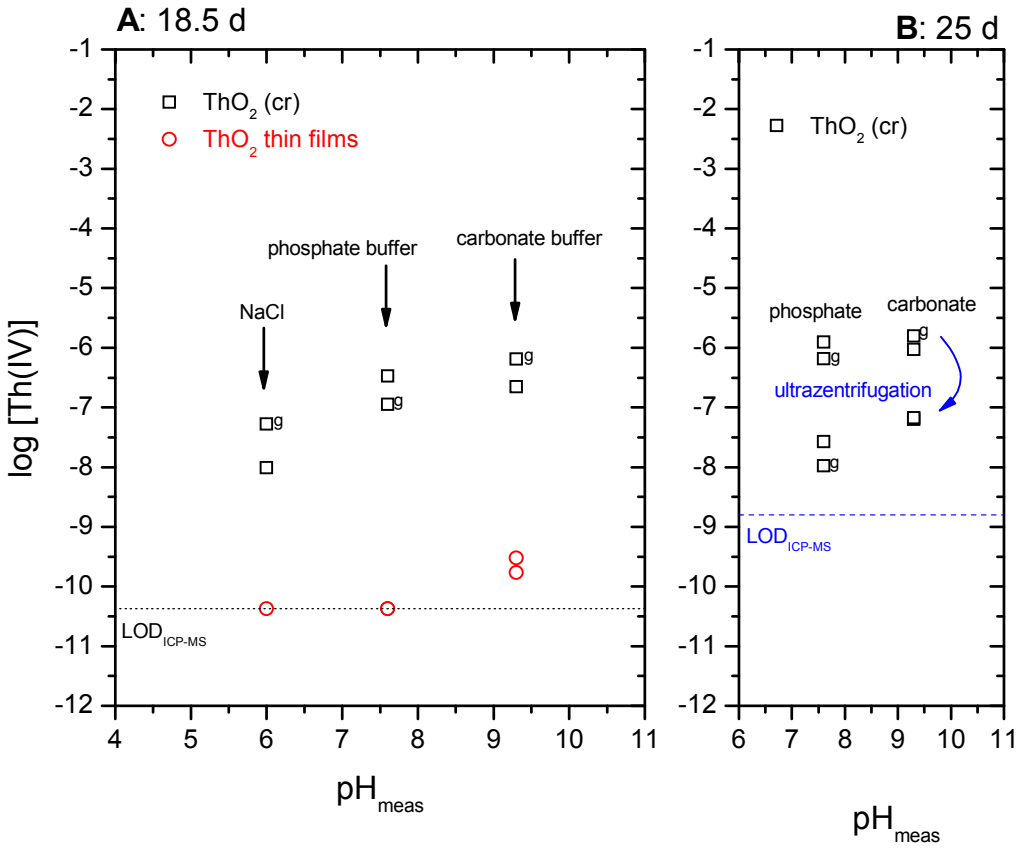

Figure 27: Solubility of ThO_2 (cr) samples in different media and leaching times (A: 18.5 d, B: 25 d). I ~ 0.01 M for all solutions. The different detection limits (LOD) for ICP-MS measurements in A and B are due to different measurement procedures for the two sample sets. Samples stored in glass vials are marked with g.

The influence of the Si content (resp. the use of glass vials or polyethylene (PE) vials) is not clear. For the non-centrifuged samples after 18 d in the solutions stored in glass vessels a Si concentration just about the detection limit is obtained (~ $4.3 \cdot 10^{-5}$ mol/L). The influence of Si on the Th concentrations in solution is small but evident. For all powder samples the measured aqueous Th concentrations (without ultracentrifugation) in the phosphate electrolyte are lower in the glass vessels. While for carbonate and chloride electrolyte the Th(aq) concentrations are higher in the glass vessels than the concentrations measured for the experiments in PE vials. This behaviour is reproduced in the sample set after 25 d.

The thin film samples are measured with AFM before and after the solubility experiments. Representative pictures for RT and 200 °C depositions before and after the solubility experiment with carbonate are shown in Figure 28. No significant differences are observed in the

morphology before and after the solubility experiment. Indeed from the ICP-MS data it can be concluded that only a very small amount (~ 10^{-4} %) of the total Th is transferred into solution.

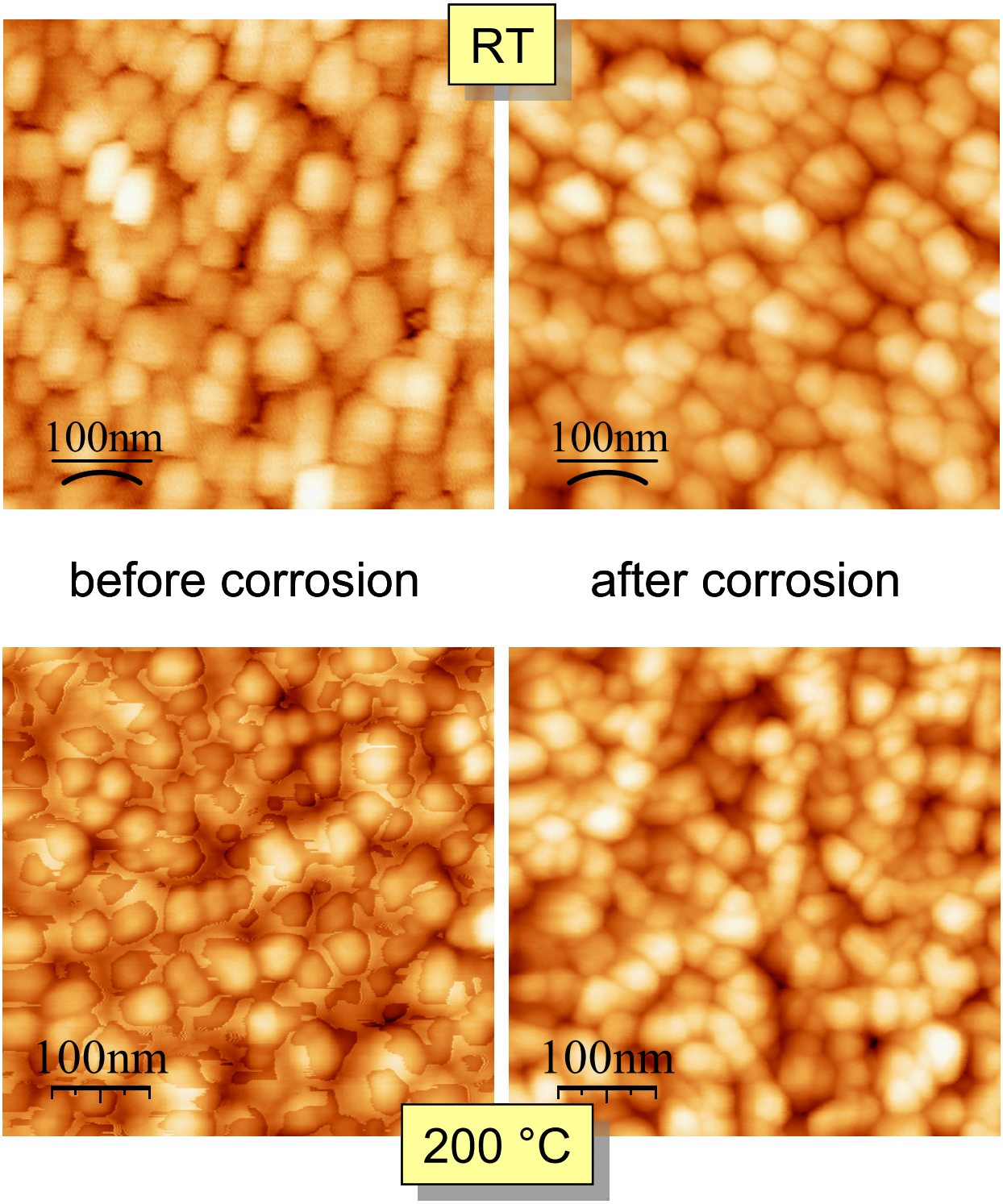

Figure 28: AFM images of ThO_2 thin films (deposited at room temperature and 200 °C) before and after a solubility experiment over 25 days in carbonate buffer.

Table 10 summarizes the AFM results (roughness, maximum height and crystallite size) for the samples used in the solubility experiments. The data for ThO_2-5 and ThO_2-7 after the experiment are thought to be representative for the surface morphology before the solubility experiment as in the phosphate medium no significant dissolution was detectable ([Th] in aqueous phase below ICP-MS detection limit). From the AFM images we also conclude that there is no precipitation of a significant amount of secondary phase (at least none with a different morphology).

The Raman investigations after the solubility experiments showed no difference between the solid phases before and after the experiment. Especially no significant phosphate signals were detected in the samples that were contacted with the phosphate buffer. Characteristic phosphate signals may be expected ~ 1072 cm^{-1} and 1119 cm^{-1} (symmetric and antisymmetric stretching modes of the P-O bond) (see for example [Cla08] and literature therein).

Table 10: Synopsis of AFM results for ThO_2 films deposited on SiO_2 glass substrates before and after the solubility experiments. All samples are measured in tapping mode.

sample	Deposition condition: T and deposition rate	rms roughness	$height_{max}$, nm	crystallite size, nm	solubility exp.
ThO_2-7 (after)	RT, low	1.17	9	~ 30	phosphate
ThO_2-8*	RT, medium	2.48	19	50 - 70	before
ThO_2-8 (after)	RT, medium	2.99	21	50 - 70	carbonate
ThO_2-5 (after)	200 °C, low	2.15	17	30 - 50	phosphate
ThO_2-6	200 °C, medium	1.77	12	30 - 60	before
ThO_2-6 (after)	200 °C, medium	3.08	20	~ 50	carbonate

* measured in contact mode

Comparing the results for the thin film samples and the bulk powder samples it seems that the thin films are not releasing a significant amount of colloidal particles into solution as it is seen for the powder samples. Despite their lower crystallinity their behaviour is much like that of ThO_2 (cr). For neither of the samples a change of the Raman spectra is observed leading to the conclusion that under the applied conditions no significant secondary phases are build up. This is also in accordance with the AFM results showing no significant morphology changes for the film surfaces after the corrosion experiment.

3.5.2 Uranium

The static batch experiments are conducted in 0.01 M NaCl, $3.3 \cdot 10^{-4}$ M phosphate buffer and 0.01 M carbonate buffer. The samples are stored at 22 ± 2 °C. Thin films of $UO_{2(+x)}$ ($4 \cdot 10^{-5}$ M to $6 \cdot 10^{-4}$ M maximum concentration in solution) on their SiO_2 or Au substrates are immersed in 5 ml, respectively 15 ml of the buffers. Aliquots of the solutions are measured after ~18 days by ICP-MS. No separation procedure (like ultracentrifugation) was applied. All experiments are conducted in PE vials but some of the substrates used for the thin films are SiO_2 glass or quartz. None of the solutions showed a Si concentration above the detection limit ($3.6 \cdot 10^{-5}$ mol/L, calculated for the original solutions). For sample SiO_2-3 the film was loosened from its substrate, therefore the particles are removed by filtration over a 0.2 µm Acrodisc filter membrane before the ICP-MS measurement. In the experiment with Au-2 an orange precipitate was obtained, which was separated before the ICP-MS measurement over a Teflon filter. Results from ICP-MS measurements are summarized in .

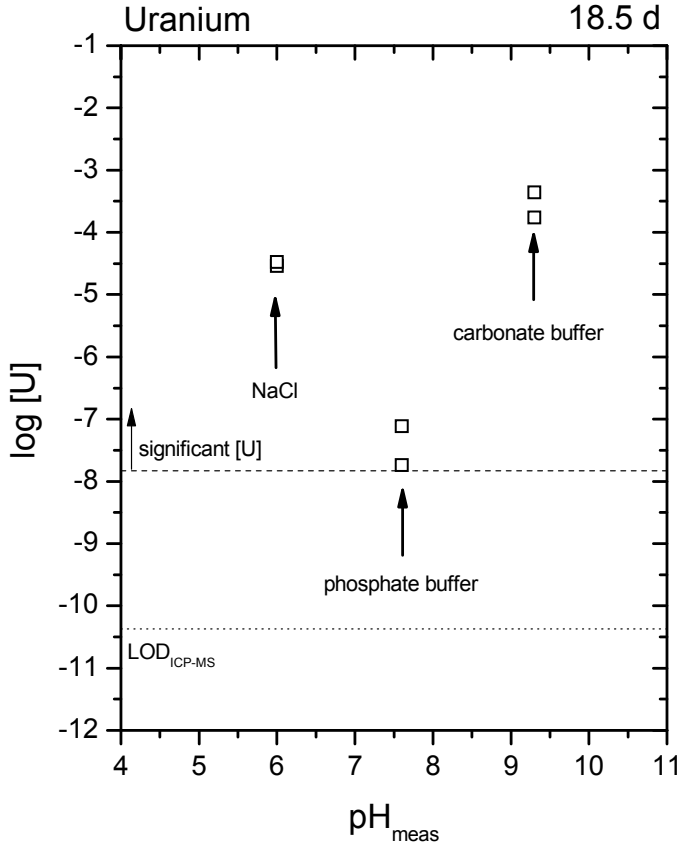

Figure 29: Solubility of $UO_{2(+x)}$ thin film samples in different media and on different substrates. I ~ 0.01 M for all solutions. The detection limit (LOD) for ICP-MS measurement of uranium is similar to that for thorium, but due to an increased uranium content (compared to Th) in the buffers and blank tests only a concentration of uranium above $1.5 \cdot 10^{-8}$ M was considered significant.

Indeed in the case of the $UO_{2(+x)}$ we deal with a corrosion phenomenon more than with a pure solubility experiment. Even under glove box conditions (O_2 < 2 ppm) usually an oxidation of U(IV) to the more soluble UO_2^{2+} is observed. Compared to the chloride and carbonate media the solubility of the uranium in the phosphate buffer is strongly decreased. This is thought to be due to the formation of at least a protective layer of a uranyl phosphate phase on the film surface, which hinders an additional oxidation and dissolution. Additional tests with Raman spectroscopy to detect and characterise such a layer (or probably secondary phase) were not successful. This may due to the low amount of material confined only to the surface. XPS measurements to detect possibly some phosphate species on the surface were not undertaken due to time limitation.

Raman spectra for samples crold1 and Au-3 after the solubility experiment in phosphate electrolyte do not show significant differences to the measurements before the solubility experiment. In both cases somewhat mixed spectra were obtained (similar before and after the solubility experiment) that do not exactly resemble UO_2 with only the T_{2g} vibration ~ 450 cm^{-1}, but are similar to the $UO_{2.0}$ reference thin film sample showing the additional double peak around 570 – 630 cm^{-1}. As example the Raman spectra for Au-3 before and after the solubility experiment are shown in Figure 30.

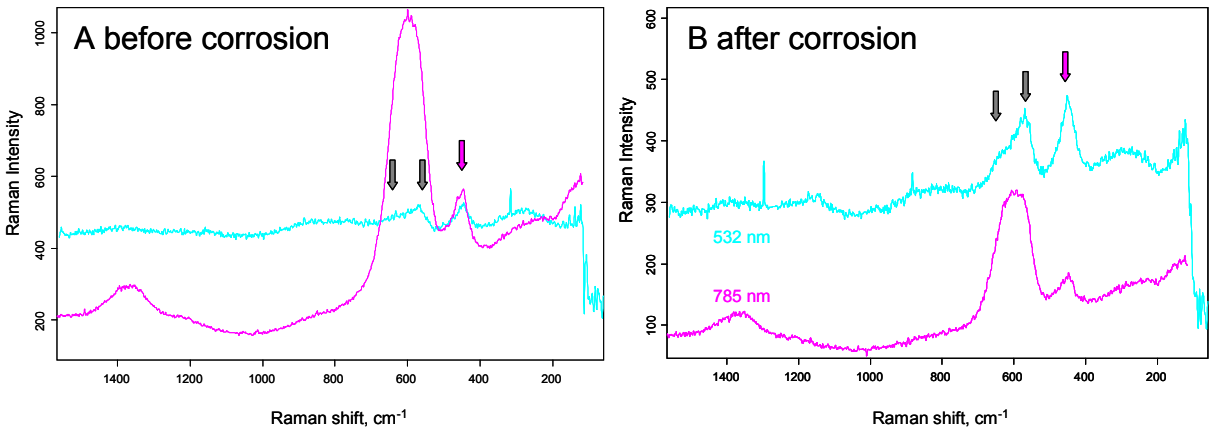

Figure 30: Raman spectra of a $UO_{2(+x)}$ thin film on gold substrate (Au-3) before (A) and after (B) the solubility experiment in the phosphate electrolyte, pH 7.6. Excitation wavelengths are 785 nm (red spectra) and 532 nm (blue spectra). The 20 x objective of the microscope is used.

In the carbonate solution both thin film samples are dissolved completely (no residues are observed by eye) and measured uranium concentrations in solution correspond to the expected values for a complete dissolution. Anyhow in the experiment with sample Au-2 (carbonate electrolyte, pH 9.3) an unexpected orange precipitate is observed. Indeed a closer inspection of the Au plate showed that there is a zone present on the back side of the substrate which is significantly different to the rest of the plate. This residue and the precipitate are characterised by Raman spectroscopy as iron phase. Raman spectroscopic measurements are shown in Figure 31 for the precipitate (a similar result was obtained for the residue on the Au plate). Comparison with literature data [Dow06, deF97, deF07] for different iron

phases / minerals leads to the conclusion that precipitate, as well as residue, are hematite, Fe_2O_3.

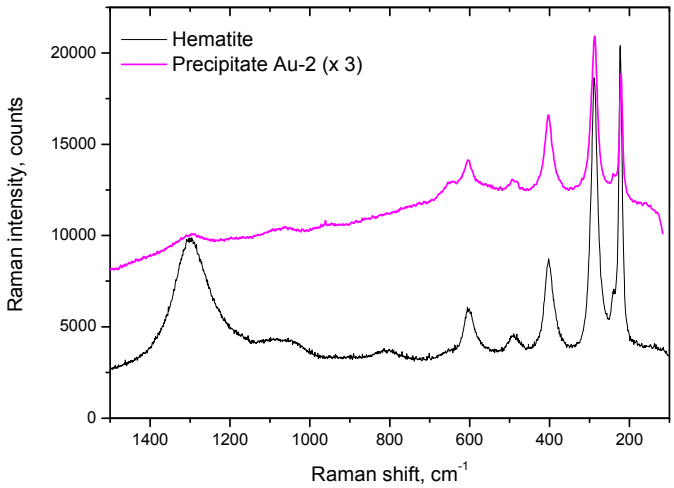

Figure 31: Raman spectra from precipitate (red) and reference spectra of hematite (black). Excitation wavelength is 785 nm.

The measured spectra and the literature spectra for comparison are plotted in Figure 31. Similar to the uranium oxide phases also for the redox sensitive iron oxides an influence of the laser irradiation on the stability of the iron phases is reported in literature [deF97, deF07]: lower iron oxides are thought to be oxidised in the high power laser spot. But as the original solubility experiment was taking place under ambient air the precipitation of hematite seems reasonable. So it is assumed that no oxidation due to the laser irradiation was seen but the original precipitate can be considered as hematite. The origin of this iron contamination of the sample is not clear.

4 Conclusions

Surface analytical techniques available at INE and ITU were evaluated for the characterisation of thin film model systems for spent nuclear fuel. These model systems are used in single effect studies designed to clarify the underlying reaction mechanisms of spent nuclear fuel behaviour under waste repository conditions.

Photoelectron spectroscopy is usually used for the surface characterisation of the thin films at ITU. The additional methods Atomic Force Microscopy and Raman spectroscopy available at INE were tested for their applicability for ThO_2 and uranium oxide films. As shown earlier for UO_2 thin films, the AFM method is, with some adaptations, as well a valuable tool for the characterisation of the surface morphology of ThO_2 thin films. It could be shown, that the tapping mode operation of the system worked well for the ThO_2 films, while the earlier used contact mode operation gave results afflicted with artefacts. This is thought to be mainly due to the fact that one deals with an insulating material in the case of ThO_2 while the semiconducting UO_2 films gave also good results with the contact mode operation. Special considera-

tions concerning the AFM set-up at INE are that the AFM is installed in the controlled area in a (at the moment open) glovebox. Practically, this allows the measurement of open radioactive samples up to 1000 times the exemption limit given by the German Radiation Protection Regulation (Strahlenschutzverordnung). Therewith the films investigated throughout this campaign (UO_2 and ThO_2) were orders of magnitude below these limits. Concerning mixed films with Pu or U-233 with an increased α-activity (planned for a future collaboration), it has to be checked whether these can be produced according to the legal exemption limits.

Raman spectroscopy is assumed an appropriate additional method for thin film characterisation. Besides the fingerprint application for identification of certain (secondary) phases, it seems interesting to follow in more detail the solid state spectroscopy path, which probably can give hints for the understanding of the structural properties of the sputter deposited films. The applicability of the surface enhanced mode needs further investigation. An appropriate method for the surface enhancement on this kind of samples is not established and assessed yet.

The solubility experiments performed throughout this experimental campaign gave, mainly due to time limitations, only preliminary results. These indicate that the ThO_2 thin films are comparable to ThO_2 (cr).

As additional technique X-ray diffraction (XRD) is used for the thin film characterisation. The advantage is that with this bulk method structural information for the entire film thickness is obtained, which gives additional and complementary information to the surface sensitive methods applied. A full understanding of the factors influencing the bulk growth in the UO_2 and ThO_2 films is not obtained yet.

Acknowledgements

D. Fellhauer and E. Soballa are acknowledged for their kind help in laboratory. M. Altmaier is acknowledged for providing the Th and U compound references and help with the solubility experiments. A. Bauer is acknowledged for XRD measurements at INE. Thanks to V. Metz for fruitful discussions and technical support.

This investigation was financially supported by Svensk Kärnbränslehantering AB (SKB) under the contract number FZK35018928(11-2008).

5 References

[Abr01] M. Abramowski, S.E. Redfern, R.W. Grimes, S. Owens, Surf. Sci. 490, 415-420 (2001)

[Age91] J.W. Ager III, D.K. Veirs, G.M. Rosenblatt, Phys. Rev. B 43, 6491-6499 (1991)

[All05] C. Alliot, B. Grambow, C. Landesman, J. Nucl. Mat. 346, 32-39 (2005)

[All87] G.C. Allen, I.S. Butler, N. Anh Tuan, J. Nucl. Mat. 144, 17-19 (1987)

[All92] M.J. Allen, N.V. Hud, M. Balooch, R.J. Tench, W. J. Siekhaus, R. Balhorn, Ultramicroscopy 42-44, 1095-1100 (1992)

[Alt05] M. Altmaier, V. Neck, R. Müller, Th. Fanghänel, Radiochim. Acta 93, 83-92 (2005)

[Alt06] M. Altmaier, V. Neck, M.A. Denecke, R. Yin, Th. Fanghänel, Radiochim. Acta 94, 495-500 (2006)

[Amm02] M. Amme, B. Renker, B. Schmid, M.P. Feth, H. Bertagnolli, W. Döbelin, J. Nucl. Mat. 306, 202-212 (2002)

[Aro07] A.K. Arora, M. Rajalakshmi, T.R. Ravindran, V. Sivasubramanian, J. Raman Spec. 38, 604-617 (2007)

[Beg90] G.M. Begun, R.G. Haire, W.R. Wilmarth, J.R. Peterson, J. Less-Com. Met. 162, 129-133 (1990)

[Biw90] B.M. Biwer, W.L. Ebert, J.K. Bates, J. Nucl. Mat. 175, 188-193 (1990)

[Bru06] J. Bruno, R.C. Ewing, Elements 2, 343 - 349 (2006)

[But88] I.S. Butler, G.C. Allen, N.A. Tuan, Appl. Spec. 42, 901-902 (1988)

[Che06] K. Chen, K.-C. Vo-Dinh, F. Yan, M.B. Wabuyele, T. Vo-Dinh, Anal. Chim. Acta 569, 234-237 (2006)

[Cla06] N. Clavier, E. du Fou de Kerniel, N. Dacheux, P. Le Coustumer, R. Drot, J. Ravaux, E. Simoni, J. Nucl. Mat. 349, 304-316 (2006)

[Cla08] N. Clavier, G. Wallez, N. Dacheux, D. Bregiroux, M. Quarton, P. Beaunier, J. Sol. St. 181, 3352-3356 (2008)

[Col84] C.A. Colmenares, Prog. Sol. St. Chem. 15, 257-364 (1984)

[Coo82] M.J. Cooper, Acta Cryst. B 38, 264-269 (1982)

[Dac04] N. Dacheux, N. Clavier, A.-C. Robisson, O. terra, F. Audubert, J.-E. Lartigue, C. Guy, C. R. Chimie 7, 1141-1152 (2004)

[Dac06] N. Dacheux, N. Clavier, J. Ritt, J. Nucl. Mat. 349, 291-303 (2006)

[Das02] S. Dash, A. Singh, P.K. Ajikumar, H. Subramanian, M. Rajalakshmi, A.K. Tyagi, A.K. Arora, S.V. Narasimhan, B. Raj, J. Nucl. Mat. 303, 156-168 (2002)

[deF07] D.L.A. de Faria, F.N. Lopes, Vib. Spec. 45, 117-121 (2007)

[deF97] D.L.A. de Faria, S. Venancio Silva, M.T.de Olivera, J. Raman Spec. 28, 873-878 (1997)

[Dem04] P. Demkowicz, J.L. Jerden Jr., J.C. Cunnane, N. Shibuya, R. Baney, J. Tulenko, Nucl. Techn. 147, 157-170 (2004)

[Dow06] R.T. Downs, The RRUFF Project: an integrated study of the chemistry, crystallography Raman and infrared spectroscopy of minerals. Program and abstracts of the 19th General Meeting of the International Mineralogical Association in Kobe, Japan, O03-13 (2006)
http://rruff.info/

[Eme94] L. Emerson, G. Cox, Micron 25, 267-269 (1994)

[Fou00] B. Fourest, T. Vincent, G. Lagarde, S. Hubert, P. Baudoin, J. Nucl. Mat. 282, 180-185 (2000)

[Gla00] J.-P. Glatz, P. Carbol, J. Cobos-Sabate, T. Gouder, F. Miserque, J. Gimenez, D.H. Wegen, in: Release of radiotoxic elements from high burn-up UO_2 and MOX fuel in a repository, Sydney, Australia (2000)

[Gou07] G. Gouadec, P. Colomban, Prog. Crystal Growth Character. Mat. 53, 1-56 (2007)

[Gou02] T. Gouder, L. Havela, Microchim. Acta 138, 207-215 (2002)

[Gra90] P.R. Graves, Appl. Spec. 44, 1665-1667 (1990)

[Gre92] I. Grenthe, J. Fuger, R.J.M. Konings, R. J. Lemire, A.B. Muller, C. Nguyen-Trung, H. Wanner, Thermodynamics of Uranium. Edited by H. Wanner, I. Forest. Elsevier Science Publ., North Holland, Amsterdam, Netherlands (1992).

[Grü92] P. Grütter, W. Zimmerman-Edling, D. Brodbeck, Appl. Phys. Lett. 60, 2741-2743 (1992)

[Gün96] H. Günzler, H.M. Heise, IR-Spektroskopie. Eine Einführung. 3. Edition, VCH, Weinheim (1996)

[Hei03] G. Heisbourg, S. Hubert, N. Dacheux, J. Ritt, J. Nucl. Mat. 321, 141-151 (2003)

[Hei04] G. Heisbourg, S. Hubert, N. Dacheux, J. Purans, J. Nucl. Mat. 335, 5-13 (2004)

[Hoe73] H.R. Hoekstra, S. Siegel, J. Inorg. Nucl. Chem. 35, 761-779 (1973)

[Hor07] I. Horcas, R. Fernandez, J.M. Gomez-Rodriguez, J. Colchero, J. Gomez-Herrero, A.M. Baro, Rev. Sci. Instr. 78, 013705 (2007)

[Hua00] B.R. Huang, K.H. Chen, W.Z. Ke, Mat. Lett. 42, 162-165 (2000)

[Hub01] S. Hubert, K. Barthelet, B. Fourest, G. Lagarde, N. Dacheux, N. Baglan, J. Nucl. Mat. 297, 206-213 (2001)

[Hub08a] S. Hubert, G. Heisbourg, Ph. Moisy, N. Dacheux, Book of Abstracts "Pu Futures-The Science" 2008, 223 (2008)

[Hub08b] S. Hubert, G. Heisbourg, N. Dacheux, Ph. Moisy, Inorg. Chem. 47, 2046-2073 (2008)

[Jeg04] C. Jegou, S. Peuget, V. Broudic, D. Roudil, X. Deschanels, J.M. Bart, J. Nucl. Mat. 326, 144-155 (2004)

[Joh05] L. Johnson, C. Ferry, C. Poinssot, P. Lovera, J. Nucl. Mat. 346, 56-65 (2005)

[Ker73] V. G. Keramidas, W.B. White, J. Chem. Phys. 59, 1561-1562 (1973)

[Las93] J.J. Laserna, Anal. Chim. Acta 283. 607-622, (1993)

[Lei74] H.D. Leigh, E.R. McCartney, J. Am. Ceramic Soc. 57, 192 (1974)

[Lop98] T. Lopez-Rios, E. Sandre, J. Raman Spec. 29, 733-737 (1998)

[Lyo98] L.A. Lyon, C.D. Keating, A.P. Fox, B.E. Baker, L. He, S.R. Nicewarner, S.P. Mulvaney, M. J. Natan, Anal. Chem. 70, 341R-361R (1998)

[Mah02] S.A. Mahmoud, Sol. St. Sci. 4, 221-228 (2002)

[Man03] D. Manara, B. Renker, J. Nucl. Mat. 321, 233-237 (2003)

[Mar66] P.G. Marlow, J.P. Russell, J.R. Hardy, Philos. Mag. 14, 409 (1966)

[McE98] R.J. McEachern, P. Taylor, J. Nucl. Mat. 254, 87-121 (1998)

[Mic76] D. Michel, M. Perez y Jorba, R. Collongues, J. Raman Spec. 5, 163-180 (1976)

[Mis01] F. Miserque, T. Gouder, D.H. Wegen, P.D.W. Bottomley, J. Nucl. Mat. 298, 280-290 (2001)

[Nec02] V. Neck, R. Müller, M. Bouby, M. Altmaier, J. Rothe, M.A. Denecke, J.I. Kim, Radiochim. Acta 90, 485-494 (2002)

[Nec03] V. Neck, M. Altmaier, R. Müller, A. Bauer, Th. Fanghänel, J.I. Kim, Radiochim. Acta 91, 253-262 (2003)

[Pal00] M.L. Palacios, S.H. Taylor, Appl. Spec. 54, 1372-1378 (2000)

[Par08] G.K. Parker, G.A. Hope, R. Woods, Col. Surf. A 325, 132-140 (2008)

[Ran08] M.H. Rand, J. Fuger, I. Grenthe, V. Neck, D. Rai, Chemical Thermodynamics of Thorium. Edited by F. Mompean, M. Illemassene, J. Perrone. OECD Publications, vol. 11 (2008)

[Rey08] A. Rey, J. Gimenez, I. Casas, F. Clarens, J. de Pablo, Appl. Geochem. 23, 2249-2255 (2008)

[Sei06] A. Seibert, Report No. JRC-ITU-TN-2006/78 (2006)

[Sei07] A. Seibert, Report No. JRC-ITU-TN-2007/81 (2007)

[Ser98] J.A. Serrano, J.-P. Glatz, E.H. Toscano, D. Papaioannou, J. Barrero, M. Coquerelle, J. All. Comp. 271-273, 573-576 (1998)

[Sho00] D.W. Shoesmith J. Nucl. Mat. 282, 1-31 (2000)

[Sho07] D.W. Shoesmith, Report No. NWMO TR-2007-03 (2007)

[Sko08] F. N. Skomurski, L.C. Shuller, R.C. Ewing, U. Becker, J. Nucl. Mat. 375, 290-310 (2008)

[Smi04] R.-E. (Lords) Smith, J. Nucl. Mat. 328, 215-224 (2004)

[Spa00] K. Spahiu, L. Werme, U.-B. Eklund, Radiochim. Acta 88, 507-511 (2000)

[Spa04] K. Spahiu, D. Cui, M. Lundström, Radiochim. Acta 92, 625-629 (2004)

[Tho74] J.A. Thornton, J. Vac. Sc. Techn. 11, 666-670 (1974)

[Tho77] J.A. Thornton, Ann. Rev. Mater. Sc. 7, 239-260 (1977)

[Van08] J. Vandenborre, A. Abdelouas, B. Grambow, Radiochim. Acta 96, 515-520 (2008)

[Vol98] V.A. Volkovich, T.R. Griffith, D.J. Fray, M. Fields, Vibr. Spec. 17, 83-91 (1998)

[Wag81] C.D. Wagner, L.E. Davis, M.V. Zeller, J. Taylor, R.M. Raymond, L.H. Gale, Surf. Interface Anal. 3, 211-225 (1981)

[Wes93] K.L. Westra, A.W. Mitchell, D.J. Thomson, J. Appl. Phys. 74, 3608-3610 (1993)

Annex A Reference Raman data from literature

Table 11: Raman shifts from literature for ThO_2 together with our own results.

		Raman shift, cm^{-1} (T_{2g})	Excitation wave-length, nm	Reference
ThO_2	single crystal	466	Ar ion laser	[Ker73]
ThO_2	Not clear	465	488.0, 496.5 or 514.5 (Ar)	[Mic76]
ThO_2	Polycrystalline sample from Th-oxalate decomposition	465	457.9, 488.0, 514.5 (Ar) or 647.1 (Kr)	[Beg90]
ThO_2	Polycrystalline sample from Th-carbonate decomposi-tion	464	482.5 (Ar)	[Das02]
ThO_2	nanocrystalline (~ 6 nm) sample from Th-carbonate decomposition	461 Broad asymmetric	482.5 (Ar)	[Das02]
ThO_2	Thorianite (RRUFF ID R060849), mineral from Malagasy Republic	~ 460 + 2 broad peaks (560 and 607) + some intensity in the range 1100 – 1600 cm^{-1}	785, 532	[Dow06]
ThO_2	Thin film (Au substrate)	458	785, 532	This work
ThO_2 (**A**)	Polycrystalline, 99.99 % (Aldrich)	465 + some intensity in the range 1100 – 1600 cm^{-1}	785, 532	This work
ThO_2 (**B**)	$Th(OH)_4$ calcined at 1100 °C	465 + some intensity in the range 1100 – 1600 cm^{-1}	785, 532	This work
$Th(OH)_4$	amorphous, precipitated from $Th(NO_3)_3$ solution, washed NO_3^- free and dried	~ 448 very broad	785, 532	This work

Table 12: Raman shifts for uranium compounds from literature and this study.

		Raman shift, cm^{-1}	vibration	Excitation wave-length, nm	Reference
UO_2		~ 445	T_{2g}		[Mar66]
UO_2	single crystal	467	T_{2g}	Ar ion laser	[Ker73]
UO_2	Polycrystalline sample from hydrolysis of U(IV) in fluoride flux	445	T_{2g}	647.1 (Kr)	[Beg90]
UO_2	single crystal and powder	445	T_{2g}	Ar ion laser	[All87]
U_4O_9 α-U_3O_8 β-U_3O_7	powders	445 broad 236, 342, 408, 480, 752, 798, 445 (broadened)	T_{2g}	Ar ion laser	[All87]
α-U_3O_8	micro crystals	236 (?), 342, 408, 480, 638, 752, 798, 888,		Ar ion laser	[But88]
UO_2	single crystal	448 1150 (electronic)	T_{2g}	514.5 (Ar)	[Gra90]

UO_2	powder	445	T_{2g}	514.5 (Ar)	[Pal00]
α-U_3O_8 γ-UO_3	powders	~ 350, 412, 483, 738, 811, 768, 846,		514.5 (Ar)	[Pal00]
UO_2	powder	445 369 (?)	T_{2g}	514 (Ar)	[Amm02]
UO_2	powder (as pellet)	445 232 1150 (electronic scattering ?)	T_{2g}	514 (Ar)	[Man03]
UO_{2+x}	powder (as pellet)	445 – 475 232 to 242, ~330, 763 to 750		514 (Ar)	[Man03]
UO_2	Uraninite (RRUFF ID R07747), mineral from Maine, USA	~ 450 ~ 600	T_{2g}	780, 532	[Dow06]
$UO_3 \cdot x\ H_2O$ $(UO_2)_8O_2(OH)_{12} \cdot 12\ H_2O$	Schoepite (RRUFF R080082), mineral from Katanga, Congo	841 854	ν_1 O-U-O sym. strech	780, 532	[Dow06]
$UO_3 \cdot 0.8\ H_2O$	Dehydrated schoepite, mineral	842	ν_1 O-U-O sym. strech	514.5 (Ar)	Biw[90]

$UO_3 \cdot 0.8\ H_2O$	Dehydrated schoepite	841	ν_1 O-U-O sym. strech		[Hoe73]
(Ca, Ba, Pb, K, Na)$U_2O_7 \cdot 5\ H_2O$	Calciouranoite (RRUFF R070022), Oktyabr'skoye Mo-U deposit, east Transbaikal region, Russia	961 793 660, 543, 470, 387, 301, 203,		780, 532	[Dow06]
$Na_2U_2O_7$	Sodium diuranate from U_3O_8 + Na-carbonate heating in air	788, 779 752, 584, 420, 313, 274, 233, 146, 117,		780	[Vol98]
UO_2	Thin film	448 577 627	T_{2g}	785, 532	This work
U_3O_8	Powder	too weak		785, 532	This work
Na-uranate $Na_2U_2O_7$	Powder	790 581, 485, 422, 344, 296, 237, 137, 118,		785, 532	This work

Ca-uranate $Ca_2U_2O_7$	Powder	793 483, 416, 366, 298, 219, 133,		785, 532	This work
schoepite	Powder	839 749 features below 600		785, 532	This work

Annex B Results from solubility experiments

Table 13: Blank samples for solubility experiments.

Name	Element / max. expected conc. ng/ml			annotation	buffer	pH	measured			conc. in sample		
	Si	**U**	**Th**				**Si**	**U**	**Th**	**Si**	**U**	**Th**
							ng/ml	ng/ml	ng/ml	mol/L	mol/L	mol/L
Glass 1	10000	-	-	SiO_2 plate in contact with electrolyte	carb	9.3	< 100	1.485	< 0.001	3.57E-05	6.239E-08	4.310E-11
Glass 2	10000	-	-	SiO_2 plate in contact with electrolyte	phos	7.6	< 100	0.145	< 0.001	3.57E-05	6.092E-09	4.310E-11
Glass 3	10000	-	-	glass in contact with electrolyte	phos	7.6	133.125	0.056	< 0.001	4.754E-05	2.353E-09	4.310E-11
Glass 4	10000	-	-	glass in contact with electrolyte	carb	9.3	235.443	0.042	< 0.001	8.409E-05	1.765E-09	4.310E-11
Glass 5	10000	-	-	glass in contact with electrolyte	NaCl	6	< 100	0.025	< 0.001	3.57E-05	1.050E-09	4.310E-11
carb	-	-	-	electrolyte in PE	carb	9.3	< 100	0.013	< 0.001	3.57E-05	5.46218E-10	4.310E-11
phos	-	-	-	electrolyte in PE	phos	7.6	< 100	0.01	< 0.001	3.57E-05	4.20168E-10	4.310E-11
NaCl	-	-	-	electrolyte in PE	NaCl	6	< 100	0.009	< 0.001	3.57E-05	3.78151E-10	4.310E-11
											background U 1.47E-08	upper limit

marked in green: concentrations below detection limit, calculated concentration is only upper limit marked in red: from the U concentrations in the blank solutions a significantly increased U concentration is defined as > $1.47*10^{-8}$ mol/L

Table 14: Thorium samples from solubility experiments.

Name	Element / max. expected conc. ng/ml			annotation	buffer	pH	measured			conc. in sample		
	Si	U	Th				Si	U	Th	Si	U	Th
							ng/ml	ng/ml	ng/ml	mol/L	mol/L	mol/L
A	10000	-	30	glass	NaCl	6	109.628	< 0.001	1.231	3.915E-05	4.202E-11	5.306E-08
B	10000	-	30	glass	Phos	7.6	143.051	< 0.001	2.638	5.109E-05	4.202E-11	1.137E-07
C	10000	-	30	glass	carb	9.3	105.592	0.482	15.163	3.771E-05	2.025E-08	6.536E-07
D	-	-	30		NaCl	6	< 100	< 0.001	0.226	3.57E-05	4.202E-11	9.741E-09
E	-	-	30		phos	7.6	< 100	< 0.001	7.841	3.57E-05	4.202E-11	3.380E-07
F	-	-	30		carb	9.3	< 100	0.217	5.155	3.57E-05	9.118E-09	2.222E-07
Cr23	1000	-	30		NaCl	6	< 100	3.862	< 0.001	3.57E-05	1.623E-07	4.310E-11
ThO_2-5	10000	-	30		phos	7.6	< 100	0.18	< 0.001	3.57E-05	7.563E-09	4.310E-11
ThO_2-6	10000	-	30		carb	9.3	< 100	4.637	0.007	3.57E-05	1.948E-07	3.017E-10
ThO_2-7	10000	-	30		phos	7.6	< 100	0.032	< 0.001	3.57E-05	1.345E-09	4.310E-11
ThO_2-8	10000	-	30		carb	9.3	< 100	0.686	0.004	3.57E-05	2.882E-08	1.724E-10
											background	
											1.47E-08	upper limit

marked in green: concentrations below detection limit, calculated concentration is only upper limit marked in red: U concentrations considered as insignificant. From the U concentrations in the blank solutions a significantly increased U concentration is defined as > $1.47*10^{-8}$ mol/L, compare table 13. So there are 2 samples (cr23 and ThO2-6) with significant U content. It is not clear from where this contamination is coming from.

Table 15: Uranium samples from solubility experiments.

Name	Element / max. expected conc. ng/ml			annotation	buffer	pH	measured			conc. in sample		
	Si	**U**	**Th**				**Si**	**U**	**Th**	**Si**	**U**	**Th**
							ng/ml	ng/ml	ng/ml	mol/L	mol/L	mol/L
SiO_2-2	10000	270	-		NaCl	6	< 100	681.832	< 0.001	3.57E-05	2.865E-05	4.310E-11
SiO_2-3	10000	270	-		NaCl	6	< 100	796.185	< 0.001	3.57E-05	3.345E-05	4.310E-11
CroId1	1000	270	-		phos	7.6	< 100	0.434	< 0.001	3.57E-05	1.824E-08	4.310E-11
Cr50	1000	270	-		carb	9.3	< 100	4130.043	0.766	3.57E-05	1.735E-04	3.30E-08
Au-2	-	270	-	iron contamination	carb	9.3	< 100	10516.308	0.035	3.57E-05	4.419E-04	1.51E-09
Au-3	-	270	-		phos	7.6	< 100	1.825	0.127	3.57E-05	7.668E-08	5.47E-09
											background	
											1.47E-08	upper limit

marked in green: concentrations below detection limit, calculated concentration is only upper limit marked in red: U concentrations considered as insignificant. From the U concentrations in the blank solutions a significantly increased U concentration is defined as > $1.47*10^{-8}$ mol/L, compare table 13. It is not clear from where the Th contamination of samples cr50, Au-2 and Au-3 is coming from.